Tellus SERIES A DYNAMIC METEOROLOGY AND OCEANOGRAPHY
PUBLISHED BY THE INTERNATIONAL METEOROLOGICAL INSTITUTE IN STOCKHOLM

How well do state-of-the-art atmosphere-ocean general circulation models reproduce atmospheric teleconnection patterns?

By DÖRTHE HANDORF* and KLAUS DETHLOFF, *Alfred Wegener Institute for Polar and Marine Research, Research Department Potsdam, Telegrafenberg A43, D-14471 Potsdam, Germany*

(Manuscript received 8 December 2011; in final form 20 September 2012)

ABSTRACT

This article evaluates the ability of state-of-the-art climate models to reproduce the low-frequency variability of the mid-tropospheric winter flow of the Northern Hemisphere in terms of atmospheric teleconnection patterns. Therefore, multi-model simulations for present-day conditions, performed for the 4th assessment report of the Intergovernmental Panel on Climate Change, have been analysed and compared with re-analysis data sets. The spatial patterns of atmospheric teleconnections are reproduced reasonably by most of the models. The comparison of coupled with atmosphere-only runs confirmed that a better representation of the forcing by sea surface temperatures has the potential to slightly improve the representation of only wave train-like patterns. Due to internally generated climate variability, the models are not able to reproduce the observed temporal behaviour. Insights into the dynamical reasons for the limited skill of climate models in reproducing teleconnections have been obtained by studying the relation between major teleconnections and zonal wind variability patterns. About half of the models are able to reproduce the observed relationship. For these cases, the quality of simulated teleconnection patterns is largely determined by the quality of zonal wind variability patterns. Therefore, improvements of simulated eddy-mean flow interaction have the potential to improve the atmospheric teleconnections.

Keywords: atmospheric teleconnections, zonal wind variability, CMIP3

1. Introduction

The extra-tropical atmospheric flow is characterised to a large extent by large-scale spatial patterns of correlated anomalies of the climate fields (e.g. pressure, temperature and precipitation) with time-varying amplitude and phase. These patterns are called atmospheric teleconnection patterns and represent a considerable portion of the low-frequency atmospheric variability on time-scales of months and longer. The existence of preferred patterns of atmospheric variability has long been recognised, starting with the pioneering work by Walker and Bliss (1932). Since then, teleconnection patterns have been estimated by numerous studies, applying different statistical methods. For example, in their seminal work, Wallace and Gutzler (1981) identified several extra-tropical Northern Hemisphere teleconnection patterns by means of correlation analysis, whereas another seminal paper by Barnston and Livezey (1987) classified the Northern Hemisphere teleconnection patterns on the basis of rotated empirical orthogonal function (EOF) analysis.

Atmospheric teleconnections determine anomalous circulation conditions occurring simultaneously over remote regions, which influence the long-range weather and its prediction. For instance, the North Atlantic Oscillation (NAO) is the dominant teleconnection pattern for the North Atlantic-European region. It is mainly represented by a seesaw between Iceland and the Azores (Hurrell, 1996) and most pronounced during winter. The NAO-index measures the phase and strength of the NAO and indicates the strength of the westerlies over the North Atlantic and Western Europe, which determines the winter climate in Europe. The Pacific/North American pattern (PNA) is the dominant teleconnection pattern for the North Pacific–North America region and appears in the form of a wave train emanating from the tropical central Pacific and propagating to North America (Dickson and Namias,

*Corresponding author.
email: doerthe.handorf@awi.de

Citation: Tellus A 2012, **64**, 19777, http://dx.doi.org/10.3402/tellusa.v64i0.19777

1976; Wallace and Gutzler, 1981). The positive phase of the PNA is related to an enhanced East Asian jet stream and an eastward shift of the jet exit region. During the negative PNA phase, a ridge over the Aleutians is associated with a westward retraction of the Pacific jet stream and blocking activity over the northern North Pacific.

On the larger scale, atmospheric teleconnections describe important aspects of the low-frequency atmospheric variability and are driven by the internal atmospheric dynamics and/or by the interaction between the atmosphere and slowly varying components of the climate system like the ocean. Additionally, external forcing, for example, changes in the greenhouse gas concentrations, can influence the spatial and temporal behaviour of teleconnection patterns. Until now, the underlying dynamical processes of atmospheric teleconnections are not yet fully understood, and an improved understanding is required to meet the challenges of seasonal to decadal predictions.

An inspection of the dominant Northern Hemisphere teleconnection patterns reveals that most of them are associated with large-scale changes in the atmospheric wave and jet stream patterns (e.g. Wallace and Gutzler, 1981; Blackmon et al., 1984; Ambaum et al., 2001; Athanasiadis et al., 2010). Hence, the basic dynamics of the teleconnection patterns is related to the dynamics of jet streams and their variability. It was found by Athanasiadis et al. (2010) that the anomaly patterns of the eddy forcing are similar to those of the related jet anomalies, which underlines the crucial role of the atmospheric eddies in maintaining the teleconnection patterns. Most teleconnection patterns appear in the form of 'standing' waves or in the form of North–South-orientated dipoles. For the 'standing' wave patterns, for example, the PNA, one likely mechanism is the propagation of planetary Rossby waves with small phase speed along atmospheric waveguides (jet streams). In particular for the origin and maintenance of dipole patterns like the NAO and the West Pacific pattern (WP), the central contribution of the high-frequency eddy feedback and synoptic wave breaking was underlined by several studies (Feldstein, 2003; Benedict et al., 2004; Franzke et al., 2004; Riviere and Orlanski, 2007; Woollings et al., 2008). Furthermore, Franzke et al. (2011a) have provided evidence that synoptic wave breaking together with tropical convection drive the evolution of the PNA. The mentioned studies suggest that synoptic wave breaking play an important role for the origin and maintenance of most atmospheric teleconnections.

Because atmospheric teleconnection patterns deliver important contributions to the low-frequency variability influencing seasonal to decadal predictability, general circulation models (GCMs) should simulate these patterns reliably. There are a few early studies on evaluating the ability of GCMs to simulate teleconnection patterns (e.g. Glowienka-Hense, 1990; Huth, 1997; Renshaw et al., 1998). Today, it becomes more widespread to include the examination of low-frequency variability in terms of teleconnections in the evaluation process of GCMs and to study their changes under future climate projections (e.g. Stephenson and Pavan, 2003; Kuzmina et al., 2005; Stephenson et al., 2006; Stoner et al., 2009; Casado and Pastor, 2012). The last two studies analysed the simulated low-frequency variability in terms of teleconnections across the multi-model ensemble of the 4th assessment report of the Intergovernmental Panel on Climate Change (IPCC AR4).

Stoner et al. (2009) analysed six teleconnection patterns of the atmosphere-ocean system, including only two regionally confined atmospheric patterns (NAO and PNA). Their index calculation procedure is based on monthly mean geopotential height data at 500 hPa for the whole year, whereas seasonal spatial patterns have been obtained by regressing the index time-series on the seasonally averaged original data. Stoner et al. (2009) evaluated the temporal variability by means of power spectra of the teleconnection indices and the seasonal spatial patterns for the period 1960–1999 for an ensemble of 22 AR4-models. The authors prove that the spatial patterns of the NAO and PNA are reproduced reasonably well by most of the models, but the models show a general tendency for the westward displacement of the southern centre of action of the NAO. Furthermore, the models are not able to reproduce the temporal characteristics of atmospheric teleconnection time-series. As the best reproducible feature of temporal behaviour, the enhanced spectral energy on inter-annual scale for the PNA time-series has been detected.

Casado and Pastor (2012) evaluated four dominant atmospheric variability patterns over the Euro-Atlantic region, including the NAO. The patterns and the associated time-series have been determined on the basis of daily mean sea level pressure data for the winter months in the period 1980–1999 for an ensemble of 16 AR4-models. The spatial variability has been evaluated by studying the intensity and location of the centres of action, and the temporal variability by analysing the probability density functions and e-folding time-scales. Casado and Pastor (2012) came to the conclusion that all of the studied models are able to reproduce the main spatial features of the four dominant North-Atlantic teleconnections patterns. For the analysed period 1980–1999, the Scandinavian pattern appears as the best reproducible North-Atlantic pattern. Regarding temporal characteristics, the characteristics of the probability density functions including shape, skewness and kurtosis have been reproduced by some models only, depending on the pattern under consideration, whereas none of the models was able to reproduce the

characteristic time scales of the North-Atlantic teleconnections patterns.

In addition to these studies, our work complements and broadens the studies of Stoner et al. (2009) and Casado and Pastor (2012). We provide a comprehensive evaluation of the nine dominant regionally confined atmospheric teleconnection patterns of the Northern Hemisphere for the dynamical active winter season on the basis of monthly mean geopotential height data at 500 hPa. The choice of monthly mean data is motivated by the fact that teleconnections occur on seasonal and longer time-scales, whereas variability at intermediate (10–20 days) and synoptic (2–6 days) time-scales exhibits distinct spatial patterns, which are not quasi-stationary ones (e.g. Athanasiadis and Ambaum, 2009).

The comprehensive evaluation of the set of nine known Northern Hemisphere teleconnection patterns has been carrying out across an ensemble of 23 available AR4 models. To allow for comparison with re-analysis data sets for the period from 1958 to 1999, we have selected present-day coupled simulations of the 20th century. The new comparison with analyses of available present-day atmosphere-only simulations from 1979 to 1999 allows us to draw some conclusions on the role of the interaction between the atmosphere and the slowly varying ocean for reproducing teleconnection patterns. Spatial variability has been evaluated in terms of location and strength of the centres of action and temporal variability in terms of comparison of time-series and comparison of spectral behaviour. For an overall estimation of the skill of the models in reproducing atmospheric teleconnections, several metrics have been proposed, which were not given before. The last part of our study goes beyond a pure evaluation of the spatial and temporal variability of the teleconnection patterns by presenting a detailed analysis of the dynamical reasons for the limited skill of the multi-model ensemble in reproducing observed atmospheric teleconnections.

The article is organised as follows: Section 2 includes the model and re-analysis data description and the description of the statistical methods for the determination of teleconnections. Sections 3 and 4 present the evaluation of the spatial patterns and temporal behaviour of teleconnections in the simulations under present-day conditions. In Section 5, dynamical reasons for limited skill of the multi-model ensemble in reproducing teleconnections are discussed. Finally, a summary and outlook is given in Section 6.

2. Data and methodology

2.1. Data and pre-processing

This study uses data from the World Climate Research Programme's (WCRP) Coupled Model Intercomparison Project phase 3 (CMIP3) multi-model data set (Meehl et al., 2007). This data set comprises the simulations performed for the IPCC AR4. We have used a suite of 23 models for which the required data were available. Table 1 lists the models and provides a brief summary of their key characteristics and introduces the used abbreviations for the models.

From the various simulations performed for the IPCC AR4, we analysed simulations of the climate of the 20th century with observed anthropogenic and natural forcing from 1958 to 1999. The outputs from all the models and scenarios were archived by the Program for Climate Model Diagnosis and Intercomparison (PCMDI; http://www-pcmdi.llnl.gov/about/index.php) at the Lawrence Livermore National Laboratory.

In addition, the available AMIP-style (Atmospheric Model Intercomparison Project) simulations from 1979 to 1999 have been analysed. For these simulations, the atmospheric component of the GCM is constrained by realistic sea surface temperature (SST) and sea-ice distributions. Thus, the AMIP experiments allow us to focus on the atmospheric model without the added complexity and freedoms of ocean-atmosphere feedbacks.

For comparison, gridded data fields for the period 1958–1999 from two re-analysis data sets have been analysed. These datasets comprise the 40-yr re-analysis ERA-40 provided by the European Centre for Medium-Range Weather Forecast (Uppala et al., 2005) and the re-analysis of the National Center for Environmental Prediction/National Center for Atmospheric Research (NCEP/NCAR) (Kalnay et al., 1996). NCEP Reanalysis Derived data are provided by the National Oceanic Atmospheric Administration (NOAA), Earth System Research Laboratory, Physical Sciences Division, Boulder, Colorado, USA, from their Web site at http://www.cdc.noaa.gov.

In this study, we investigate the teleconnection patterns for the mid-tropospheric circulation of the dynamically active season of the Northern Hemisphere. Therefore, we analyse the gridded geopotential height fields at 500 hPa (Z_{500}) from 20°N to 90°N for the boreal winter months December, January, February (DJF). To emphasise the low-frequency variability patterns, a simple filtering is achieved by using monthly mean data. Further pre-processing steps include the calculation of anomaly fields by removing the mean seasonal cycle and linear trends. For the comparison of data sets, for example, calculation of Taylor diagrams, all model data were projected via linear interpolation to a common $2.5^\circ \times 2.5^\circ$ grid.

2.2. Determination and evaluation of atmospheric teleconnections

For the calculation of the teleconnection patterns and indices the EOF analysis has been applied (e.g. Preisendorfer,

Table 1. Summary of information on the CMIP3 models used in this study. The abbreviations for each model are used throughout the paper

Model	Abbreviations	Atmosphere	Ocean	Coupling
BCCR-BCM2.0 Bjerknes Centre for Climate Research, Norway	BCCR	$1.9 \times 1.9°$	$0.5-1.5 \times 1.5°$	No flux adjustment
CCSM3 NCAR, USA	NCARcc	$1.4 \times 1.4°$	$0.3-1.0 \times 1.0°$	No flux adjustment
CGCM3.1 (T47) Canadian Centre for Climate Modeling and Analysis	CCCT47	$2.8 \times 2.8°$	$1.9 \times 1.9°$	No flux adjustment
CGCM3.1 (T63) Canadian Centre for Climate Modeling and Analysis	CCCT63	$1.9 \times 1.9°$	$0.9 \times 1.4°$	No flux adjustment
CNRM-CM3 Meteo-France/Centre National de Recherches Meteorol	CNRM	$1.9 \times 1.9°$	$0.5-2.0 \times 2.0°$	No flux adjustment
CSIRO Mk3.0 CSIRO Atmospheric Research, Australia	CSIRO0	$1.9 \times 1.9°$	$0.8 \times 1.9°$	No flux adjustment
CSIRO Mk3.5 CSIRO Atmospheric Research, Australia	CSIRO5	$1.9 \times 1.9°$	$0.8 \times 1.9°$	No flux adjustment
ECHAM5/MPI-OM Max Planck Institute Hamburg, Germany	MPI	$1.9 \times 1.9°$	$1.5 \times 1.5°$	No flux adjustment
FGOALS-g1.0 Institute of Atmospheric Physics, China	IAP	$2.8 \times 2.8°$	$1.0 \times 1.0°$	No flux adjustment
GFDL CM2.0 US Dept. of Commerce/NOAA/GFDL, USA	GFDL0	$2.0 \times 2.5°$	$0.3-1.0 \times 1.0°$	No flux adjustment
GFDL CM2.1 US Dept. of Commerce/NOAA/GFDL, USA	GFDL1	$2.0 \times 2.5°$	$0.3-1.0 \times 1.0°$	No flux adjustment
GISS-AOM NASA/Goddard Institute for Space Studies, USA	GISSaom	$3 \times 4°$	$3 \times 4°$	No flux adjustment
GISS-EH NASA/Goddard Institute for Space Studies, USA	GISSeh	$4 \times 5°$	$2 \times 2°$	No flux adjustment
GISS-ER NASA/Goddard Institute for Space Studies, USA	GISSer	$4 \times 5°$	$4 \times 5°$	No flux adjustment
INGV-SXG Instituto Nazionale di Geofisica e Vulcanologia, Italy	INGV	$1.1 \times 1.1°$	$1-2 \times 2°$	No flux adjustment
INM-CM3.0 Institute for Numerical Mathematics, Russia	INMCM3	$4 \times 5°$	2×2.5	Annual mean flux adjustment of water, no adjustment for heat/momentum
IPSL CM4 Institut Pierre-Simon Laplace, France	IPSL	$2.5 \times 3.75°$	$2 \times 2°$	No flux adjustment
MIROC3.2(hires) Center for Climate System Research, Nat. Institute for Environ. Studies, and Frontier Research Center, Japan	MIROh	$1.1 \times 1.1°$	$0.2 \times 0.3°$	No flux adjustment
MIROC3.2(medres) Japan	MIROm	$2.8 \times 2.8°$	$0.5-1.4 \times 1.4°$	No flux adjustment
MRI CGCM2.3.2 Meteorological Research Institute, Japan	MRI	$2.8 \times 2.8°$	$0.5-2.0 \times 2.5°$	Monthly climate flux adjustment for heat, water, momentum (12° S–12° N)
PCM NCAR, USA	NCARpcm	$2.81 \times 2.81°$	$0.5-0.7 \times 1.1°$	No flux adjustment
UKMO HadCM3 Hadley Centre/ Met Office, UK	UKMOcm	$2.5 \times 3.75°$	$1.25 \times 1.25°$	No flux adjustment
UKMO HadGEM1 Hadley Centre/ Met Office, UK	UKMOgem	$1.3 \times 1.9°$	$0.3-1.0 \times 1.0°$	No flux adjustment

1988; Hannachi et al., 2007). In the framework of EOF analysis, the anomaly field $\overrightarrow{X'}(j,t)$ is projected onto the space spanned by the EOFs:

$$\overrightarrow{X'} = \sum_{j=1}^{J} \alpha_j'(t)\overrightarrow{e_j'}. \quad (1)$$

Here $\overrightarrow{e_j'}, (j = 1, \ldots, J)$ are the EOFs which represent the spatial patterns. The time-dependent amplitude $\alpha_j'(t)$of $\overrightarrow{e_j'}$is called the jth principal component (PC) of the time-series. The EOFs are the eigenvectors $\overrightarrow{e_j'}$of the covariance matrix of the field $\overrightarrow{X'}$. The corresponding eigenvalues are proportional to the amount of variance accounted for by each eigenvector. Before calculating the covariance matrix, equal-area weighting is ensured by multiplying the fields with the square root of the cosine of latitude. All EOF patterns are re-normalised by the square root of the corresponding eigenvalues. Thus, the corresponding PC time-series a_j(t) are standardised (cf. Von Storch and Zwiers, 1999).

In general, the EOF analysis yields spatial patterns which resemble some structures of patterns obtained by the more straightforward correlation analysis (e.g. Wallace and Gutzler, 1981). Basis vector rotation are often applied to EOFs with the aim to get more localised patterns with a better separation of the EOF for each spatial point which are closer to the patterns found by correlation analysis. Therefore, we apply such a rotated EOF analysis (REOF) to the 10 leading EOF patterns, using varimax rotation (Richman, 1986) which is common in atmospheric sciences.

By means of the EOF analysis, information about the temporal evolution of the teleconnection patterns is obtained. The corresponding PC time-series can be further analysed by time-series analysis. Here, we apply the wavelet analysis (e.g. Torrence and Compo, 1998). The wavelet analysis provides information about the scales as well as about the time of appearance of characteristic structures. The global wavelet power spectrum is equivalent to the common power spectrum with the main difference of the inherent, scale-adapting averaging over scale (frequency) bands. Furthermore, the wavelet transformation offers the possibilities for filtering.

The significance of the local and global wavelet power spectra has been tested by comparison to the spectra of a corresponding red noise process which are obtained by fitting a first-order autoregressive process to the analysed time-series. Significant differences between observed and corresponding red noise spectra are determined by means of a χ^2-test applied for the calculation of confidence levels. Torrence and Compo (1998) used this concept for the establishing of significance levels and confidence intervals for the local as well as global wavelet power spectrum.

Attention has to be paid to the choice of the wavelet, because the results of the wavelet transformation are dependent on the characteristics of the selected wavelet. In this investigation we used the Morlet wavelet which is well localised in the frequency domain and well-suited for filtering. The used wavelet software is available at URL: http://paos.colorado.edu/research/wavelets/.

To quantify similarity between different atmospheric teleconnection patterns Taylor diagrams (Taylor, 2001) have been used. A Taylor diagram delivers a compact summary of pattern statistics in terms of pattern correlation, root-mean-square difference and ratio of variances. The pattern correlation is defined as the common linear (Pearson) correlation coefficient between variables at identical locations on two different maps. Before calculating pattern correlation and spatial variances equal-area weighting has been ensured.

3. Atmospheric teleconnection patterns – spatial structure

The atmospheric teleconnection patterns have been obtained by a REOF analysis of the 10 leading EOF patterns for the ERA40 re-analysis data for the winter (DJF) Z_{500} fields from 1958 to 1999. Nine of the resulting 10 leading rotated patterns have been named according to similar patterns, given by the NOAA Climate Prediction Center (http://www.cpc.ncep.noaa.gov/data/teledoc/telecontents.shtml). The patterns are displayed in Fig. 1.

Over the North-Atlantic/Eurasian area, the NAO and the East Atlantic pattern (EA) have been determined as the most dominant patterns. Additionally, two wave train-like patterns, the East Atlantic/Western Russia pattern (EA/WR) and the Scandinavia pattern (SCAN), appear. The most dominant patterns in the Pacific-North America area are the PNA and the WP, whereas the Tropical/Northern Hemisphere pattern (TNH) and the East Pacific/North Pacific pattern (EP/NP) are of minor importance. Furthermore, a pattern with a circumpolar structure, the Polar/Eurasia pattern (POL) has been determined. The explained variance of each pattern varies between 14%and 6%, the exact values are given in Table 2. The corresponding patterns obtained from the NCEP/NCAR re-analysis data set are very similar with pattern correlation >0.99 for all patterns. A detailed description of these patterns is given in Panagiotopoulos et al. (2002).

3.1. Taylor plots

By means of Taylor plots, Figs. 2 to 5 display the performance of all CMIP3 models in reproducing the spatial patterns of the major teleconnections NAO, EA, PNA and WP. The Taylor plots for the remaining patterns (EA/WR, SCAN, TNH, EP/NP, POL) can be found in the supplementary material. In each of the Figs. 2 to 5, the left panels show the comparison for all available CMIP3-models (23 models) for the period from 1958 to 1999, the right panels show the comparison for all models for which CMIP3 and AMIP3 runs are available (13 models) for the period from 1979 to 1999. First, the performance for the shorter period is generally worse. If considering e.g. the NAO pattern, 20 out of 23 CMIP3 models have pattern correlations larger than 0.7 for the period 1958–1999, but only 7 out of 13 AMIP3/CMIP3 models have pattern correlations larger than 0.7 for the period 1979–1999. Second, the comparison of the AMIP3 and CMIP3 runs for the later period 1979–1999 reveals no improvement in reproducing the spatial structure of the patterns for almost all patterns for the AMIP3 runs, except for the PNA pattern. For the PNA, 10 out of 13 models have better or equal pattern correlations for the AMIP3 runs compared to

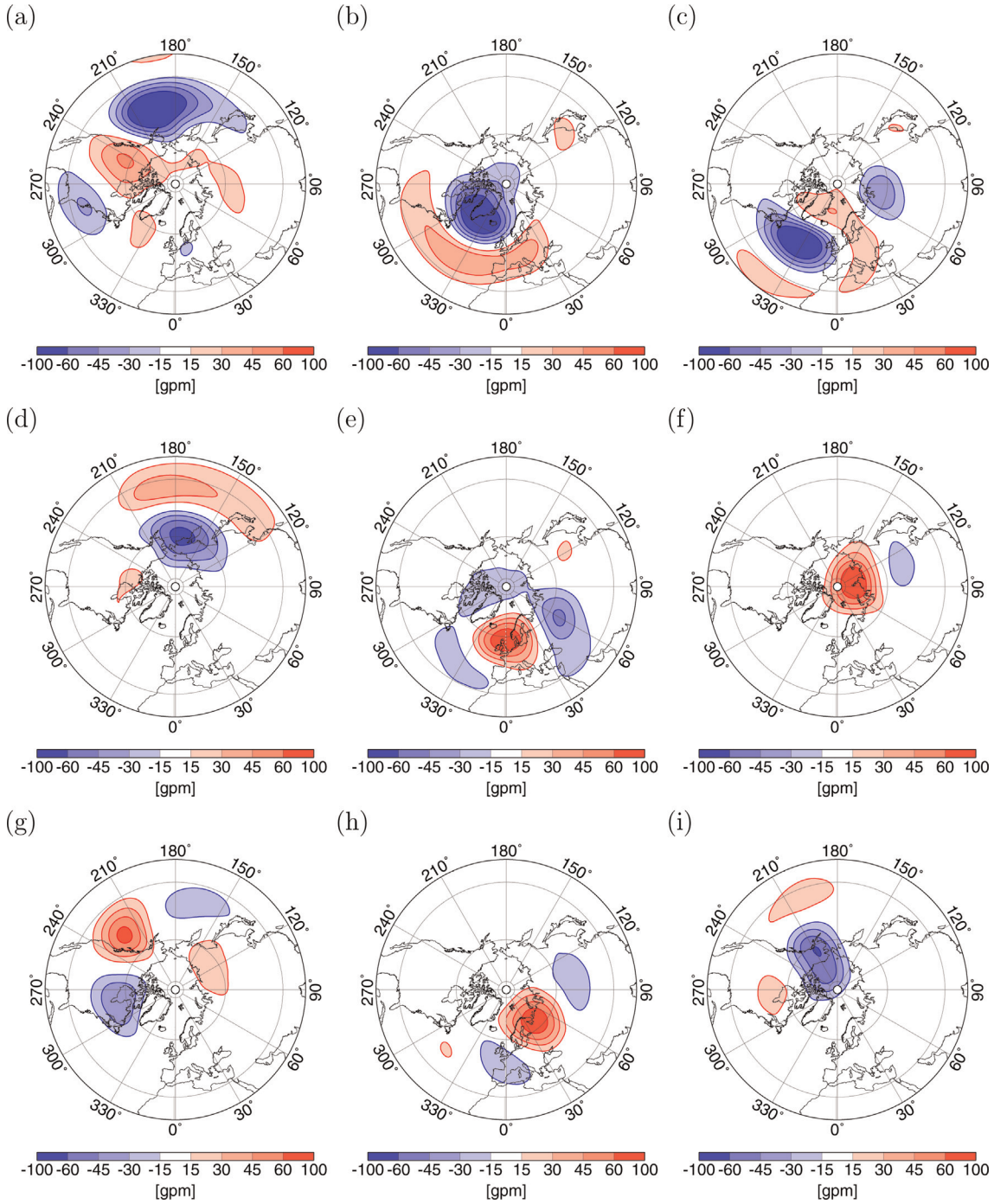

Fig. 1. Teleconnection patterns determined by rotated EOF analysis of fields of Z_{500} ERA40 re-analysis, DJF from 1958 to 1999. (a) PNA (13.7% explained variance), (b) NAO (12.8%), (c) EA (9.8%), (d) WP (7.9%), (e) EA/WR (7.8%), (f) POL (6.6%), (g) TNH (6.2%), (h) SCAN (6.0%), (i) EP/NP (5.7%). For explanations of abbreviations see Table 2.

those of the CMIP3 runs. Third, it is striking that the CMIP3 models reproduce the most dominant NAO and PNA patterns best. The intra-ensemble spread is much larger for the other patterns. For a detailed discussion of these findings see subsection 3.3.

3.2. Limits in simulating the spatial structure of teleconnections

The potentially realisable statistical agreement between simulated and observed spatial teleconnection patterns is

Table 2. Summary of used abbreviations for teleconnection patterns

Abbreviation	Name of teleconnection pattern	Explained variance, DJF Z_{500} data ERA40, 1958–1999
PNA	Pacific/North American pattern	13.7%
NAO	North Atlantic Oscillation	12.8%
EA	East Atlantic pattern	9.8%
WP	West Pacific pattern	7.9%
EA/WR	East Atlantic/West Russia pattern	7.8%
POL	Polar/Eurasia pattern	6.6%
TNH	Tropical/Northern Hemisphere pattern	6.2%
SCAN	Scandinavia pattern	6.0%
EP/NP	East Pacific/North Pacific pattern	5.7%

limited due to the internally generated climate variability differing among the models. Therefore, the exact reproduction of the spatial pattern and, in particular, the exact phasing of the corresponding temporal behaviour cannot be expected. To estimate the limits of the expected agreement between the simulated and observed spatial structure of teleconnections available ensemble simulations have been analysed. They comprise the CMIP3-simulations of ECHAM5/MPI-OM (4 runs), NCAR CCSM3 (8 runs), CCCma CGCM3.1 (T47) (5 runs), MIROC3.2(medres) (3 runs), MRI-CGCM2.3-2a (3 runs) and GFDL CM2.1 (3 runs).

The spatial patterns of the individual ensemble members have been compared to each other. The normalised statistics for each teleconnection pattern have been computed between pairs of ensemble members (see Taylor, 2001). To get the full range of standard deviations, two points are plotted for each pair of ensemble members in the Taylor plot, one considering the first realisation as the reference and the other considering the second realisation considered as the reference. Thus, overall 12/56 points are plotted for the 4/8-member ensemble shown in Figs. 6 and 7. The scatter of the points is related to the unforced internally generated climate variability. Fig. 6 displays the normalised pattern statistics for CMIP3 runs from 1958 to 1999 for the NAO and the two ensembles of ECHAM5/MPI-OM runs and NCAR CCSM3 runs. The mean of the intra-ensemble correlations amounts to 0.94 for both ensembles. For the NAO, the spread of the points is more radially directed which indicates that the unforced model variability affects mainly the pattern amplitude. This holds for all six ensembles. In contrast, the spread of the points for the PNA pattern (Fig. 7) displays more spread in azimuthal angle indicating that internal model variability leads to larger variations in the phasing of the centres of action of the PNA wave train. To summarise, Table 3 presents the mean intra-ensemble correlations for all available ensembles and all patterns. The bold values give the maximal attainable correlation which lies between 0.83 for the POL and 0.96 for the NAO pattern.

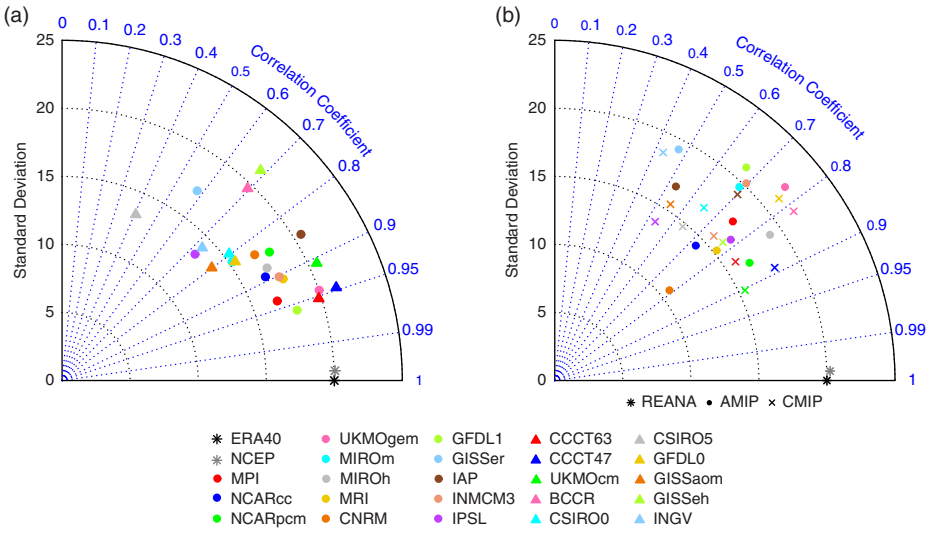

Fig. 2. Taylor plots for NAO of fields of Z_{500} CMIP3/AMIP3 model runs and NCEP/NCAR and ERA40 re-analysis, DJF. (a) CMIP3 from 1958 to 1999, (b) CMIP3/AMIP3 from 1979 to 1999.

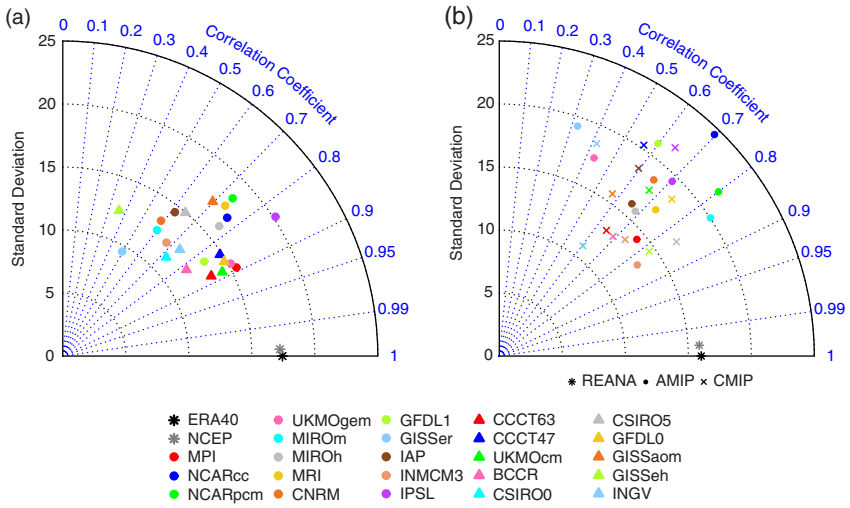

Fig. 3. Taylor plots for EA of fields of Z_{500} CMIP3/AMIP3 model runs and NCEP/NCAR and ERA40 re-analysis, DJF. (a) CMIP3 from 1958 to 1999, (b) CMIP3/AMIP3 from 1979 to 1999.

3.3. *Evaluating model skill*

To evaluate the skill of a model in reproducing a teleconnection pattern, the correlation and the RMS error have to be taken into account. Among the variety of existing skill scores taking into account these two measures, but with different weights, the following score, introduced by Taylor (2001), has been used:

$$S = \frac{4(1+R)^4}{(\widehat{\sigma_f} + 1/\widehat{\sigma_f})^2 (1+R_0)^4} \qquad (2)$$

R is the correlation coefficient, $\widehat{\sigma_f} = \sigma_f/\sigma_r$ with σ_f and σ_r are the standard deviations of the test field f and the reference field r, respectively. The above-defined skill score S depends on R_0, the maximal attainable correlation which measures the potentially realisable statistical agreement between simulated and observed teleconnection patterns. Thus, the skill score definition takes into account the noise associated with internally generated unforced model variability. R_0 has been selected according to the maximal values of the mean intra-ensemble correlations for each pattern, given in Table 3. For $\widehat{\sigma_f} \to 1$ (that means the model variance approaches the observed ones) and $R \to 1$ the skill score approaches unity ($S \to 1$). Skill decreases to zero for $R \to -1$ or model variance approaches zero or infinity.

The skill score S in eq. (2) has been selected because it increases the penalty for low correlation. Thus, errors in the exact phasing of the centres of action of the

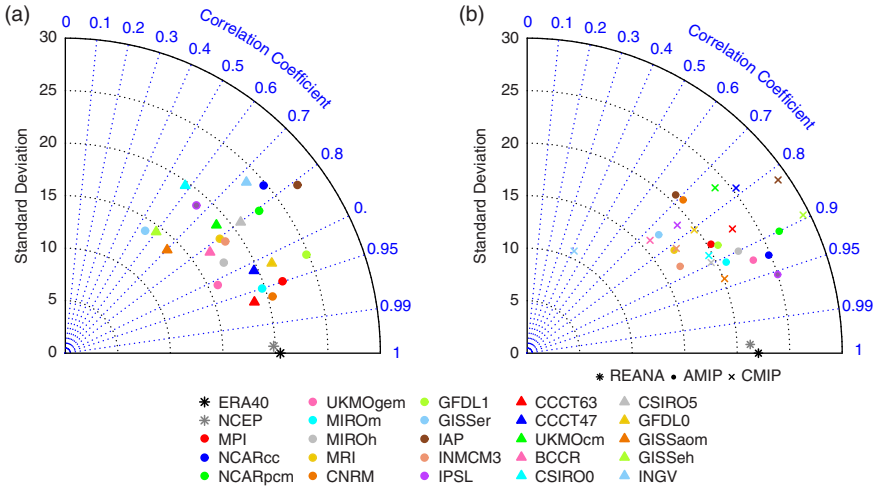

Fig. 4. Taylor plots for PNA of fields of Z_{500} CMIP3/AMIP3 model runs and NCEP/NCAR and ERA40 re-analysis, DJF. (a) CMIP3 from 1958 to 1999, (b) CMIP3/AMIP3 from 1979 to 1999.

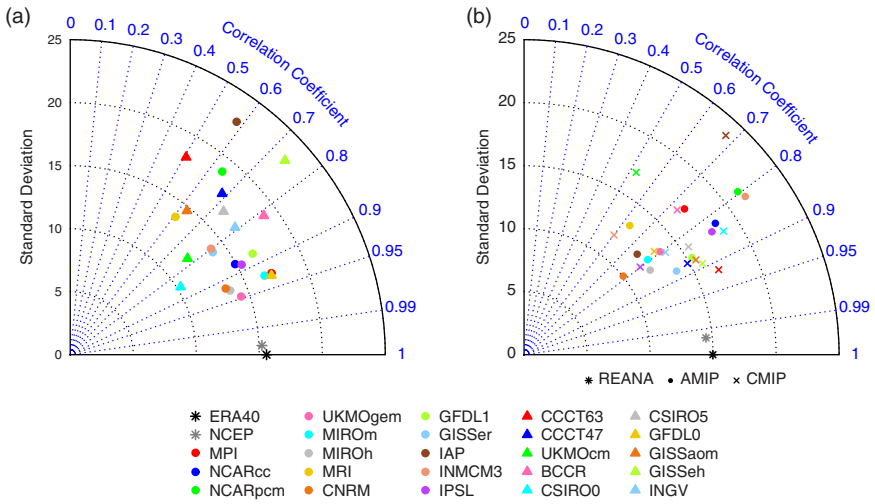

Fig. 5. Taylor plots for WP of fields of Z_{500} CMIP3/AMIP3 model runs and NCEP/NCAR and ERA40 re-analysis, DJF. (a) CMIP3 from 1958 to 1999, (b) CMIP3/AMIP3 from 1979 to 1999.

teleconnection patterns resulting in erroneous directions of the large-scale flow are penalised. Fig. 6 in the supplementary material displays the patterns statistics for the NAO pattern for the period from 1958 to 1999 (23 CMIP3-models) and for the period from 1979 to 1999 (13 CMIP3/AMIP3 models) with drawing the skill score isolines defined by eq. (2) with R_0 according to Table 3.

Table 4 shows the skill scores ranges for the CMIP3 runs from 1958 to 1999, for the CMIP3 runs from 1979 to 1999 and for the AMIP3 runs from 1979 to 1999. The generally worse performance of CMIP3 simulations for the shorter period is expressed by lower mean skill scores for all patterns. Comparison of the last two columns of Table 4 and Fig. 6 in the supplement reveals no improvement in reproducing the spatial structure of the NAO pattern for the AMIP3 runs, whereas the better reproduction of the spatial structure of the PNA pattern is expressed by a mean skill score of 0.81. Five out of 13 models have skill scores larger than 0.9 for the AMIP3 runs from 1979 to 1999. Over the North Atlantic-European sector, the spatial structures of the EA/WR and SCAN patterns are better reproduced for the AMIP3 runs than for the CMIP3 runs from 1979 to 1999. Coupled CMIP3 models reproduce the most dominant NAO and PNA patterns best. In particular, 5 and 7 out of 23 CMIP3 model simulations for the long period have skill scores larger than 0.9 for the NAO and PNA pattern respectively. Furthermore, the reproduction of the WP and SCAN patterns is of similar quality for the comparison period 1958–1999.

Our results support the findings of Stoner et al. (2009) and Casado and Pastor (2012) that the spatial patterns of the most important teleconnections are reproduced reasonably well by most of the models. Despite the different method of calculation, almost all models capable in

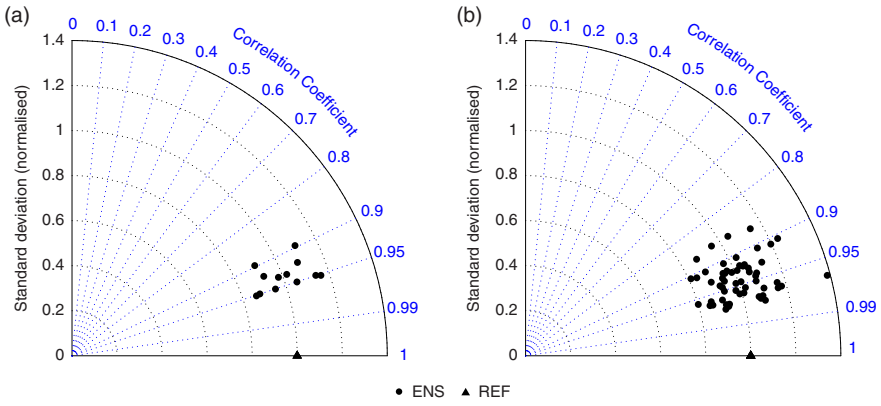

Fig. 6. Taylor plots for the normalised pattern statistics within a multi-member ensemble of simulations of the NAO pattern at Z_{500} for DJF, CMIP3 from 1958 to 1999. (a) Four-member ensemble of ECHAM5/MPI-OM1, (b) Eight-member ensemble of NCAR CCSM3.

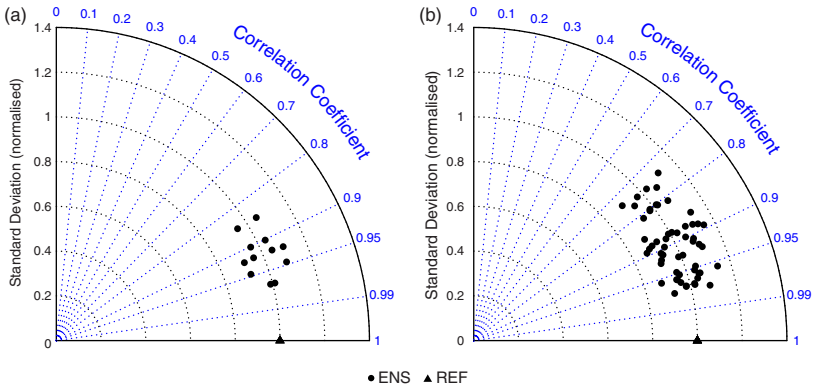

Fig. 7. Taylor plots for the normalised pattern statistics within a multi-member ensemble of simulations of the PNA pattern at Z_{500} for DJF, CMIP3 from 1958 to 1999. (a) four-member ensemble of ECHAM5/MPI-OM1, (b) eight-member ensemble of NCAR CCSM3.

simulating the winter NAO- and PNA-pattern mentioned by Stoner et al. (2009) are among the models that we detected as the models which are best reproducing the spatial patterns of NAO and PNA. Furthermore, the general tendency for the westward displacement of the southern centre of action of the NAO, described by Stoner et al. (2009) has been confirmed. Comparisons with the results of Casado and Pastor (2012) for the North-Atlantic teleconnections NAO, SCAN, EA, EA/WR prove the good quality of the pattern reproduction. In our study, the spread over the ensemble is larger since the ensembles differ. Our study reveals the NAO as the best reproducible North-Atlantic pattern for the CMIP3 runs for the period 1958–1999. According to the skill scores given in Table 4 the SCAN pattern is the best reproducible North-Atlantic pattern for the CMIP3 runs for the period 1979–1999 in agreement with Casado and Pastor (2012), although their analyses is based on daily data.

The comparison of the AMIP3- and CMIP3-ensembles for the short period from 1979 to 1999 suggests (see, e.g. Kushnir et al., 2002) that the influence of the forcing by SST anomalies on the spatial structure of the extra-tropical atmospheric variability patterns is rather small compared to internally generated variability. Only three patterns (EA/WR, SCAN, PNA) have slightly increased ensemble means of skill scores for the AMIP3 ensemble compared to the CMIP3 ensemble runs for the same period 1979–1999. This suggests that the correct representation of the forcing by SST anomalies has the potential to impact the quality of the simulated spatial patterns of wave-train like teleconnections only.

Recently, the misrepresentation of observed tropical SST changes in coupled model simulations has been discussed (Shin and Sardeshmukh, 2011). For the CMIP3 ensemble, a negative bias of the annual mean SST up to $-2K$ and larger has been estimated not only over the tropical Pacific, but also over the North Pacific and North Atlantic (Fig. 4 of Reichler and Kim, 2008). Therefore, we cannot decide, whether the slight improvement of the simulated spatial structures of wave-train like patterns under prescribed SST-forcing is attributed to the better representation of the tropical or the mid-latitude SST anomalies.

Table 3. Mean intra-ensemble correlations for all ensembles and all patterns. For abbreviations of models see Table 1

	MPI	NCARcc	CCCT47	MIROCm	MRI	GFDL1
Pattern	4 runs	8 runs	5 runs	3 runs	5 runs	3 runs
PNA	0.92	0.89	0.93	0.95	0.94	**0.95**
NAO	0.94	0.94	0.94	**0.96**	0.89	0.91
EA	**0.91**	0.86	0.88	0.90	0.91	0.80
WP	**0.93**	0.81	0.71	0.92	0.85	0.84
EA/WR	0.77	**0.84**	0.81	0.81	0.82	0.71
POL	0.56	**0.83**	0.74	0.73	0.76	0.79
TNH	0.60	0.70	0.44	0.66	0.59	**0.84**
SCAN	0.81	0.84	0.79	0.86	0.85	**0.90**
EP/NP	**0.93**	0.85	0.86	0.84	0.77	0.83

Bold: Maximal attainable correlation.

Table 4. Skill score ranges (mean ± standard deviation) for the multi-model ensemble of CMIP3 1958–1999, CMIP3 1979–1999 and AMIP3 1979–1999, respectively

Pattern	CMIP3 1958–1999	CMIP3 1979–1999	AMIP3 1979–1999
PNA	0.74 ± 0.21	0.71 ± 0.19	0.81 ± 0.15
NAO	0.73 ± 0.20	0.58 ± 0.19	0.57 ± 0.13
EA	0.66 ± 0.20	0.56 ± 0.16	0.58 ± 0.18
WP	0.73 ± 0.21	0.72 ± 0.19	0.71 ± 0.11
EA/WR	0.67 ± 0.20	0.55 ± 0.18	0.68 ± 0.22
POL	0.79 ± 0.29	0.72 ± 0.24	0.70 ± 0.20
TNH	0.55 ± 0.27	0.59 ± 0.19	0.59 ± 0.19
SCAN	0.71 ± 0.15	0.59 ± 0.11	0.68 ± 0.14
EP/NP	0.65 ± 0.22	0.62 ± 0.17	0.60 ± 0.15

It has long been known that tropical SST anomalies can force stationary wave train patterns (Hoskins and Karoly, 1981). Whether tropical SST anomalies, in particular anomalies related to El Niño-Southern oscillation (ENSO), amplify existing internal variability patterns like the PNA pattern or generate new patterns has long been discussed. Meanwhile the existence of an additional ENSO-forced mid-latitude pattern distinct from the PNA pattern has been proven (Straus and Shukla, 2002). Further evidence was given by the study of Yu et al. (2009), revealing that the PNA-related atmospheric diabatic heating is located outside the tropics over the eastern Pacific as a collocated Rossby wave source. But the insensitivity of the PNA pattern to tropical diabatic heating does not rule out that the tropical Pacific atmospheric heating anomalies induce energy transports towards North America and thus contribute to the appearance of the stationary wave pattern of PNA for particular combination of the phases of ENSO and Pacific Decadal Oscillation (Yu et al., 2007; Yu and Zwiers, 2007).

In view of the above-described results, we conclude that a better representation of the SST forcing has the potential to improve (at least slightly) the representation of wave-train like atmospheric teleconnection patterns.

3.4. Performance metrics for atmospheric teleconnection patterns

The calculated skill scores for all patterns and all models have been summarised in a metric describing the ability of the models in reproducing the spatial structure of the atmospheric teleconnection patterns.

The left panel of Fig. 8 displays the performance metric for the period from 1958 to 1999 (23 CMIP3-models) for all teleconnection patterns. In general, the models show a tendency for higher skill scores for the Pacific patterns. There are three models (UKMO HadGEM1, ECHAM5/MPI-OM1, GFDL CM2.1) which reproduce the Atlantic as well as the Pacific patterns well. Some models show large discrepancies in their ability to reproduce the patterns for the Atlantic or the Pacific sectors. UKMO HadCM3 and NCAR PCM reproduce the Atlantic patterns much better than the Pacific ones, whereas CNRM-CM and MIROC3.2(medres) reproduce the Pacific patterns much better.

The comparison of available AMIP3- and CMIP3 runs for the shorter period from 1979 to 1999 (see Fig. 8, right) confirmed the better reproduction of the PNA pattern for the AMIP3 runs since 11 out of 13 models have larger skill scores. Furthermore, the discrepancies in reproducing the patterns in the Atlantic or the Pacific sectors are confirmed for the NCAR PCM, CNRM-CM and MIROC3.2(medres) models. Additionally, the GFDL CM2.1 model and the MRI-CGCM2.3-2a model display larger differences in capturing the Atlantic and Pacific patterns than for the longer period. In detail, GFDL CM2.1 has much higher skill scores for the Pacific patterns, whereas CNRM-CM has slightly higher scores for the Atlantic patterns.

4. Teleconnection patterns – temporal behaviour

The temporal behaviour of the observed teleconnection patterns for the period 1958–1999 has been analysed by a time-frequency method, called the wavelet transformation. Fig. 9 shows the wavelet power spectra of the time-series of the NAO- and PNA-patterns, respectively. For the period 1958–1999, the NAO time-series displays a preferred timescale of about 8 yr since the late 1960s. The variations on the mentioned timescale exceed the 95% confidence level of a corresponding red noise process for the local as well as for the global (not shown) wavelet power spectrum. But due to the shortness of the analysed time-series including only a few realisations of the quasi-decadal signal the statistical significance of global wavelet power spectrum has to be interpreted with care. Indeed, the studies by Hurrell and Van Loon (1997), Handorf et al. (1999), Wunsch (1999), Marshall et al. (2001) and Barbosa et al. (2006) who analysed the full period of the respective NAO index (e.g. from 1864 up until today for the station-based

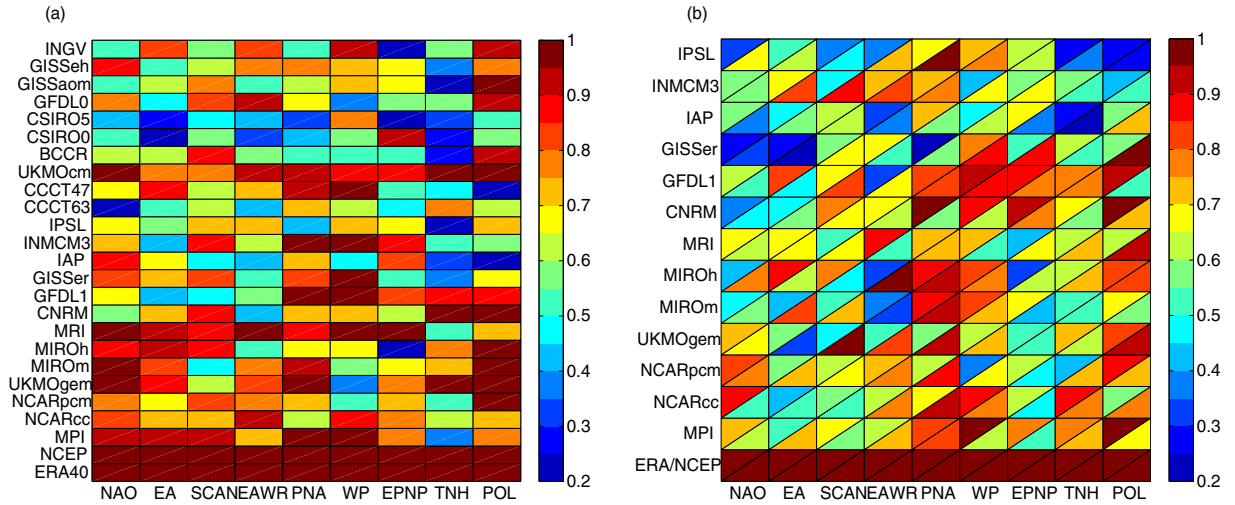

Fig. 8. Metric for teleconnection patterns of fields of Z_{500}, skill score S according to eq. (2). (a) CMIP3 from 1958 to 1999, all patterns, (b) AMIP3 and CMIP3 from 1979 to 1999, all patterns. In each rectangle the lower triangle gives the value for the AMIP3 run and the upper that of the CMIP3 run.

index), estimated a slightly red spectrum with broadband, though not significant, features on inter-annual (2–3 yr) and quasi-decadal time-scales (8 yr). Therefore no preferred time-scale is evident over the full NAO period. Time-frequency methods (e.g. Hurrell and Van Loon, 1997; Handorf et al., 1999) highlight in detail the dominant variations on inter-annual (2–3 yr) scale in the late 19th and early 20th centuries, while the quasi-decadal variations are dominant over the latter half of the 20th century. This intermittent behaviour of the NAO with enhanced spectral energy in different frequency bands is confirmed by wavelet analyses of the reconstructed NAO-index over 1659–1997 (Wanner et al., 2001).

A similar intermittent behaviour can be determined for the PNA time-series as well. For the analysed period from 1958 to 1999 in Fig. 9 enhanced wavelet power has been detected for periods of 2–4 yr with locally, but not globally statistical significance. This is in accordance with spectral analyses performed by e.g. Yu et al. (2009) and Gan et al. (2007).

The wavelet power spectra in Fig. 10 show the spectral behaviour of the NAO and PNA time-series of two models

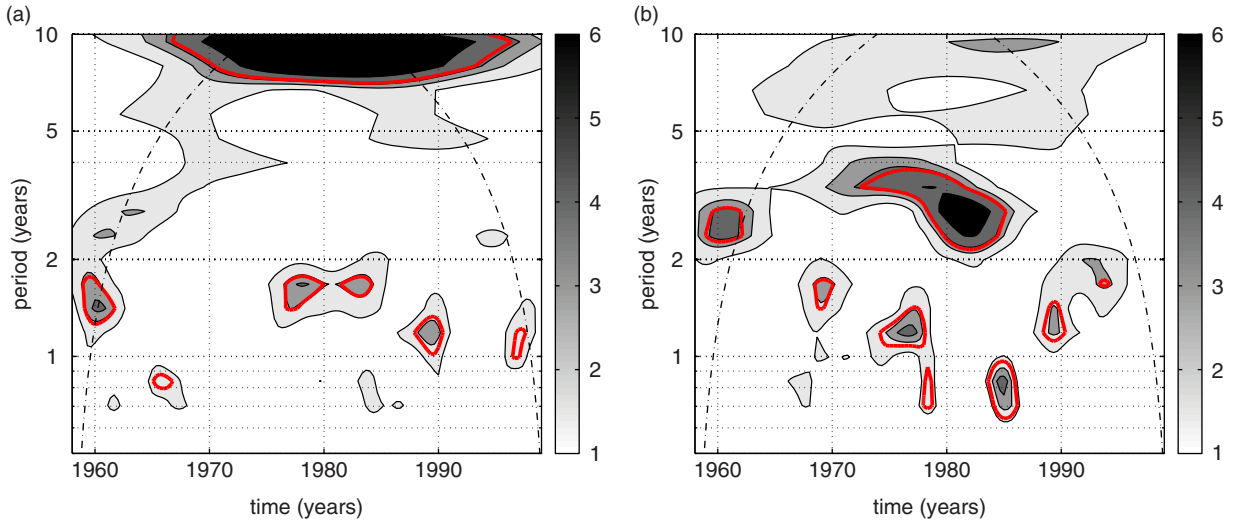

Fig. 9. Wavelet power spectra of time-series of teleconnection patterns at Z_{500}. ERA40 re-analysis, DJF from 1958 to 1999. (a) NAO-index, (b) PNA-index. The wavelet transformation was performed with the Morlet wavelet. At both ends, dash-dotted lines separate regions where edge effects become important. The thick red contour envelopes areas of greater than 95% confidence for a corresponding red noise process with lag-one autocorrelation-coefficients of 0.19 (NAO) and 0.22 (PNA), respectively.

which simulates the corresponding spatial patterns very well. For both, the ECHAM5/MPI-OM and UKMO HadGEM1 model, the NAO and PNA time-series display the characteristic intermittent behaviour. For the NAO time-series of the CMIP3 runs, enhanced spectral energy is detected for periods about 2 yr for the ECHAM5/MPI-OM model and for periods about 3–4 and 6–7 yr for the UKMO HadGEM1 model. Despite the significant areas seen in the local wavelet power spectra, only the variations on the 6–7 yr timescale for the UKMO HadGEM1 model exceed the 95% confidence level when considering the global wavelet power spectra.

For the simulated PNA time-series, the time-scales of enhanced wavelet power range from 2 to 5 yr. These signals are statistical significant on the 95% confidence level both, locally and globally, and show a better agreement with those detected for the re-analysis data, especially for the AMIP3 runs (not shown here, but compare the figures and discussion below).

These example wavelet analyses illustrate the internally generated climate variability differing among the models. Therefore the reproduction of the exact phasing of the teleconnection indices cannot be expected, as visible in the Taylor plots for the unfiltered time-series for NAO and PNA, presented in the supplementary material.

An important aspect of the temporal behaviour of teleconnections is the frequency behaviour of the corresponding time-series. Here, the behaviour in frequency

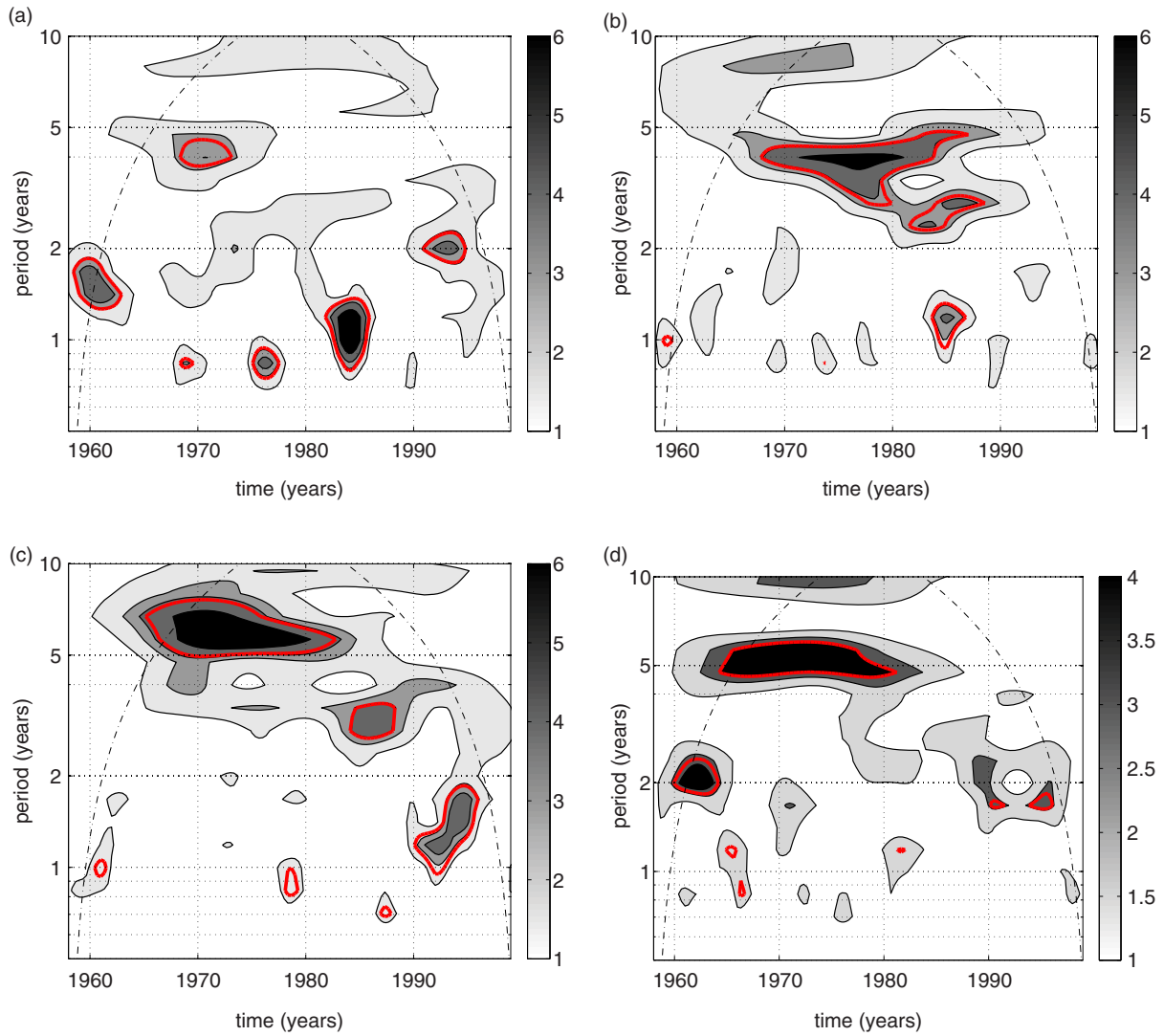

Fig. 10. Wavelet power spectra of time-series of teleconnection patterns at Z_{500}. CMIP3 runs of ECHAM5/MPI-OM (a, b) and UKMO HadGEM1 (c, d), DJF from 1958 to 1999. (a, c) NAO-index, (b, d) PNA-index. For further explanations see Fig. 9. The corresponding red noise processes have lag-one autocorrelation-coefficients of 0.06 (NAO, ECHAM5/MPI-OM), 0.15 (PNA, ECHAM5/MPI-OM), 0.21 (NAO, UKMO HadGEM1) and 0.16 (PNA, UKMO HadGEM1), respectively.

space is studied by means of wavelet transformation. The Figs. 11 to 13 display the global wavelet spectra for unfiltered and filtered time-series of the NAO and PNA-patterns. We filtered the NAO time-series on quasi-decadal periods (7–15 yr) and the PNA time-series on inter-annual periods (2–4 yr) because the respective time-series determined from re-analysis data exhibit enhanced power in these frequency bands.

In general, the models are not able to capture the observed frequency behaviour for the coupled runs. For the NAO time-series, most models display more spectral energy than observed on inter-annual scales and only a few models (CCCma CGCM3.1(T63) UKMO HadCM3, IPSL CM4) display the observed enhanced energy at quasi-decadal scale, but with smaller magnitude than for the observed NAO time-series. For the PNA time-series, the enhanced spectral energy on inter-annual scales (2–4 yr) is captured by many models, even though mostly with smaller magnitude. Some models show large energy on quasi-decadal scale, not present in the observed spectrum. For the atmosphere-only runs, the reproduction of the spectral peak at 2–4 yr is considerably improved for the majority of models. As discussed at the end of section 3.3 this is probably related to the more realistic representation of the forcing by SST anomalies within the AMIP3 model set-ups.

In the study of Stoner et al. (2009) a similar power spectrum method was applied to evaluate the temporal variability of simulated atmospheric teleconnections, but their index calculation procedure was based on monthly mean data for the whole year, and thus, the analysed period range includes annual and sub-annual behaviour. The authors arrived at the same conclusion as our study, namely that the models are not able to reproduce the temporal characteristics of atmospheric teleconnection time-series. In accordance with our study, Stoner et al. (2009) detected as the best reproducible feature of temporal behaviour the enhanced spectral energy on inter-annual scale for the PNA time-series.

5. Dynamical reasons for limited skill of the CMIP3 ensemble in reproducing teleconnections

It has long been recognised that the major teleconnection patterns are related to the mean planetary wave patterns and hence to the variability of the atmospheric jet streams (e.g. Wallace and Gutzler, 1981; Blackmon et al., 1984). This leads Athanasiadis et al. (2010) even to a new definition of extra-tropical teleconnection patterns in terms of zonal wind variability patterns separately in the North-Atlantic and North-Pacific sectors. These patterns are characterised by changes in the latitudinal position or a strengthening/weakening of the North-Atlantic and North-Pacific jets. The patterns are broadly consistent with their traditionally defined counterparts like NAO, PNA, EA or WP. For the other patterns EA/WR, SCAN, TNH, EP/NP and POL such a strong relation has not been estimated.

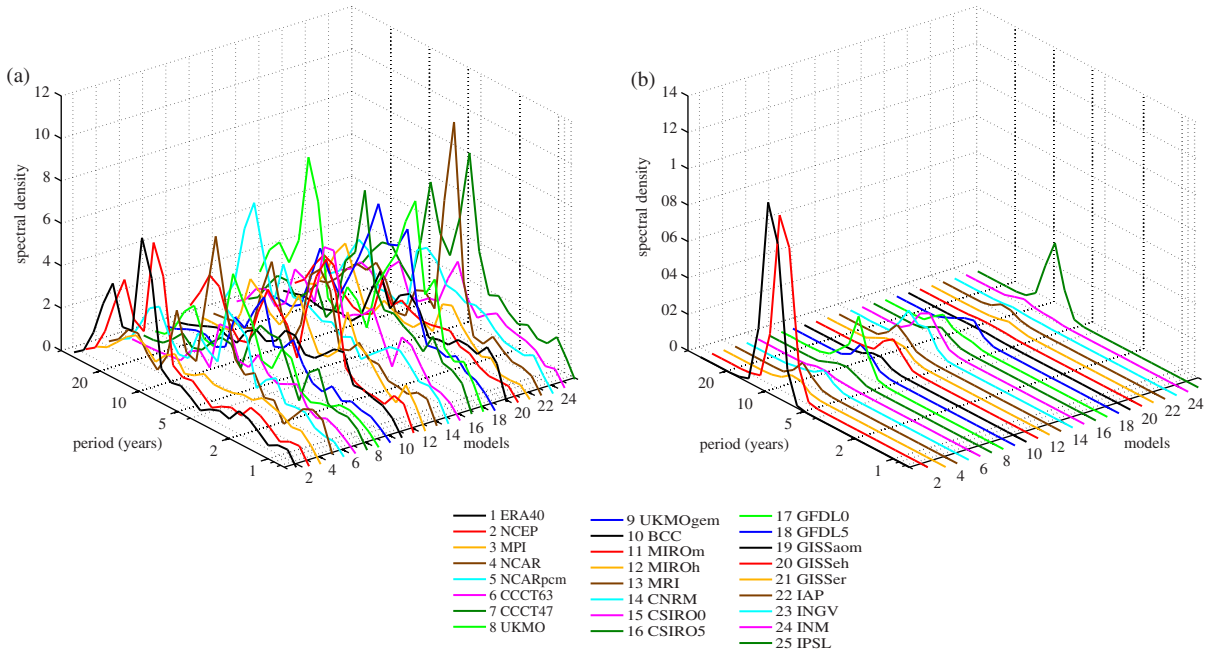

Fig. 11. Global wavelet spectra of unfiltered and filtered NAO-index at Z_{500}. CMIP3 model runs and NCEP/NCAR and ERA40 re-analysis, DJF from 1958 to 1999. (a) unfiltered, (b) bandpass-filtered 7–15 yr. The wavelet transformation and filtering was performed with the Morlet wavelet.

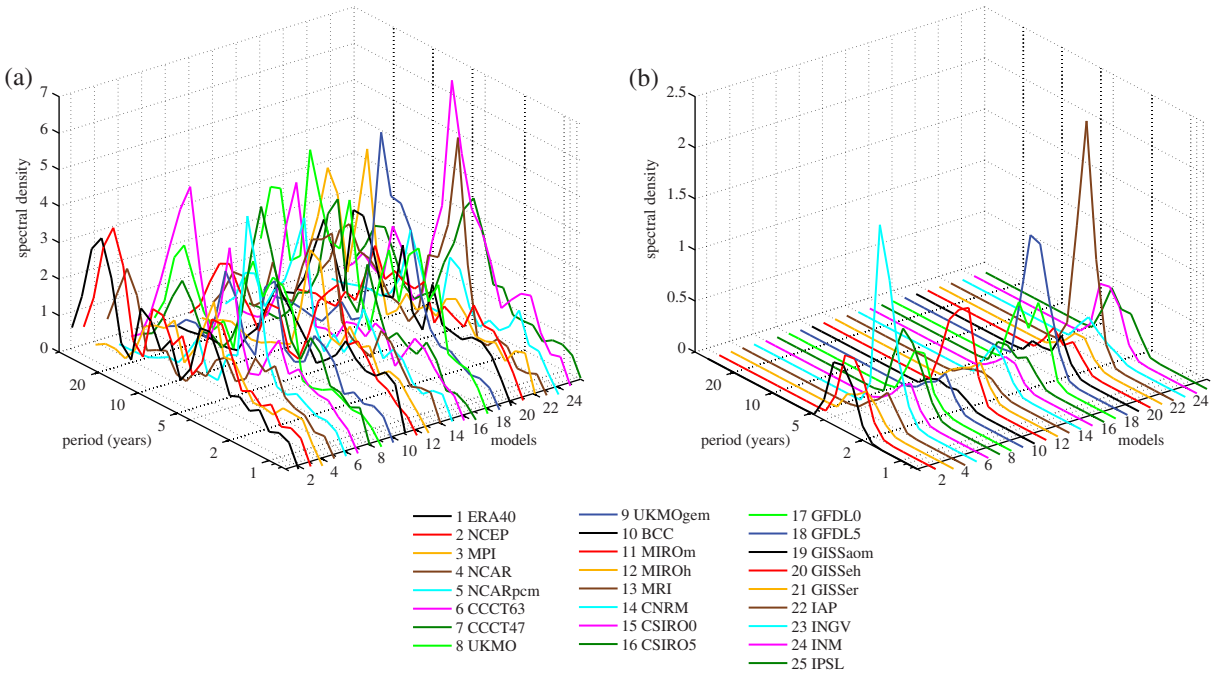

Fig. 12. Global wavelet spectra of unfiltered and filtered PNA-index at Z_{500}. CMIP3 model runs and NCEP/ NCAR and ERA40 reanalysis, DJF from 1958 to 1999. (a) unfiltered, (b) bandpass-filtered 2–4 yr. The wavelet transformation and filtering was performed with the Morlet wavelet.

5.1. Observed relation between major teleconnection patterns and zonal wind variability

The figures in the top row of Figs. 14–17 illustrate the relation of the four major teleconnection patterns NAO, EA, PNA and WP to the jet variability for the ERA-40 reanalysis monthly mean winter (DJF) data from 1958 to 1999 at the height of the jet maximum (250 hPa). The jet variability is characterised by the patterns of zonal wind variability which have been determined by an EOF analysis

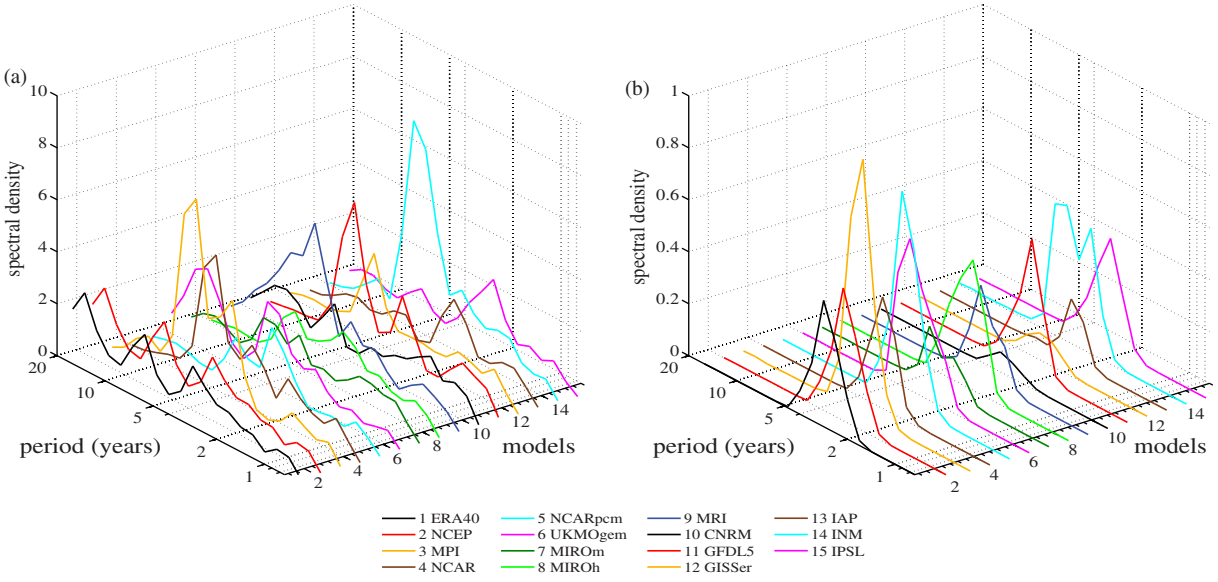

Fig. 13. Global wavelet spectra of unfiltered and filtered PNA-index at Z_{500}. AMIP3 model runs and NCEP/NCAR and ERA40 reanalysis, DJF from 1979 to 1999. (a) unfiltered, (b) bandpass-filtered 2–4 yr. The wavelet transformation and filtering was performed with the Morlet wavelet.

of the zonal wind field u at 250 hPa for the Atlantic ($-120°$–$60°$W, 20°–90°N) and Pacific (150°–240°W, 20°–90°N) sector separately. The first three columns of Figs. 14–17 display from left to right the teleconnection patterns, the regression patterns of the global geopotential height field at 500 hPa onto the sectoral zonal wind PCs at 250 hPa, and the regression patterns of the global zonal wind field at 250 hPa onto sectoral zonal wind PCs at 250 hPa. The latter patterns display changes in the positions of the Atlantic and Pacific jets (Regression onto ATL-u-PC1/PAC-u-PC2) and in the strength of the two jets (Regression onto ATL-u-PC2/PAC-u-PC1).

The regression patterns at 500 hPa are very similar to the teleconnection patterns, underlining the close relation of the NAO (EA) patterns to variations in the position (intensity) of the Atlantic atmospheric jet and of the PNA (WP) patterns to variations in the intensity (position) of the Pacific jet. Thus, the four most important teleconnection patterns NAO, EA, PNA and WP are dynamically consistent with the sectoral zonal wind variability patterns. The atmospheric zonal flow is mainly determined by two processes, described by Vallis and Gerber (2008). The first process is the transport of angular momentum by the thermally direct Hadley circulation. The arising subtropical jet is located at the edge of the Hadley cell over the subtropics where the meridional temperature gradient tends to be largest and is characterised by a baroclinic structure. The second process is the convergence of eddy momentum flux over the regions of baroclinic instability (e.g. Vallis, 2006, for more details). The jets related to this mechanism are eddy-driven jets and located at mid-latitudes. The atmospheric eddy-mean flow feedback acts to make this jet more barotropic, leading to the extension of the eddy-driven jet down through the troposphere. In the real atmosphere, both types of jets are often co-existing. This is confirmed for the North Pacific winter jet (e.g. Nakamura et al., 2004), whereas over the North Atlantic in winter, the subtropical and eddy-driven jets are generally separated (e.g. Li and Wettstein, 2012). The study by Li and Wettstein (2012) related the PNA pattern mostly to subtropically influenced Pacific jet changes, whereas the eddy-driven signatures of jet variability over the North-Atlantic and North-Pacific are similar to the zonal wind anomalies connected with the NAO and WP pattern, respectively.

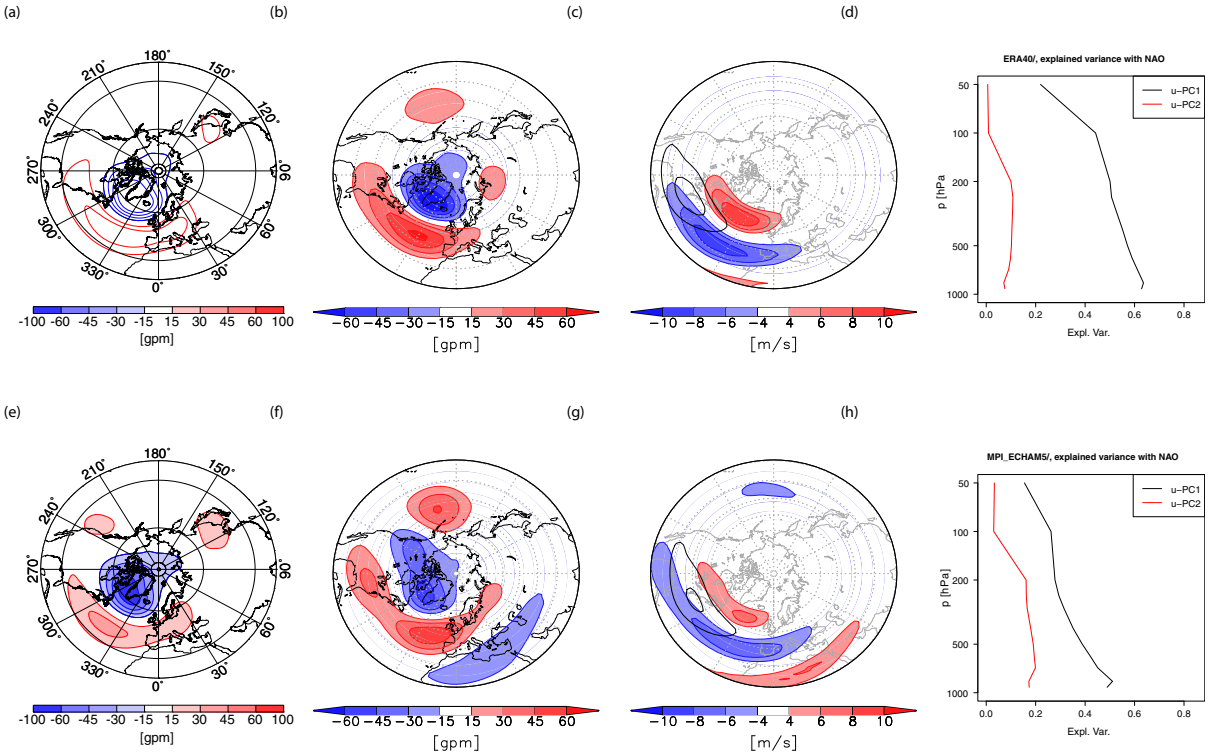

Fig. 14. Summary of the NAO patterns and their relation to ATL-u-EOF1 for ERA40 re-analysis (a–d) and ECHAM5/MPI-OM (e–h). DJF-data from 1958 to 1999. From left to right: the NAO pattern (a, e); the regression pattern of the global geopotential height field at 500hPa onto ATL-u-PC1 at 250hPa (b, f); the regression pattern of the global zonal wind field at 250hPa onto ATL-u-PC1 at 250hPa (colours with overlaid Atlantic mean jet) (c, g); the vertical profile of explained variance between the NAO-index and the sectoral ATL-u-PC1 at each height (d, h).

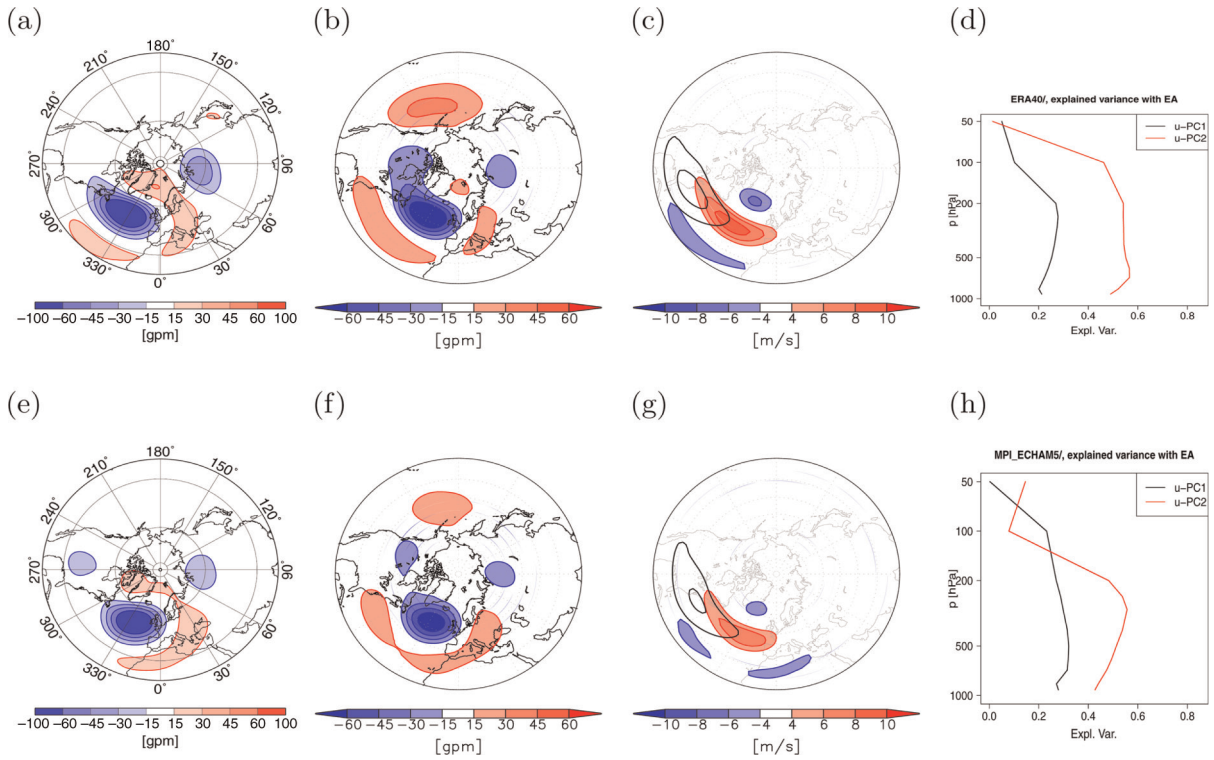

Fig. 15. Summary of the EA patterns and their relation to ATL-*u*-EOF2 for ERA40 re-analysis (a–d) and ECHAM5/MPI-OM (e–h). DJF-data from 1958 to 1999. From left to right: the EA pattern (a, e); the regression pattern of the global geopotential height field at 500hPa onto ATL-*u*-PC2 at 250hPa (b, f); the regression pattern of the global zonal wind field at 250hPa onto ATL-*u*-PC2 at 250hPa (colours with overlaid Atlantic mean jet) (c, g); the vertical profile of explained variance between the EA-index and the sectoral ATL-*u*-PC2 at each height (d, h).

The vertical profiles in the last column of Figs. 14 to 17 summarises the vertical structure of the relationship between the teleconnection patterns and zonal wind variability throughout the troposphere and lower stratosphere by showing the explained variance between the teleconnection index (determined at 500 hPa) and the sectoral *u*-PCs at each height (as introduced in Wettstein and Li, submitted to J. Climate). The most pronounced vertical structures are found for the NAO and PNA. For the NAO pattern, the profile of the explained variance revealed a maximum in the lower troposphere just above the boundary layer and decreasing values above. For the PNA pattern, the profile of the explained variance revealed a clear maximum in the upper troposphere at the jet core height (about 250–200 hPa).

These profiles are supposed to be dynamically connected to the jet-type. For eddy-driven jets, the net eddy forcing of the mean flow leads to flow deceleration at upper levels and flow acceleration at lower levels. In this case, a typical profile of explained variance between a teleconnection index and a sectoral *u*-PC is supposed to have its maximum in the lower troposphere. Otherwise, a characteristic profile of explained variance describing variability of the subtropical jet should have its maximum at the jet core height in the upper troposphere (see also the argumentation in Wettstein and Li, submitted to J. Climate). The profiles of explained variance shown in the top rows of Figs. 14 to 17 for the re-analysis data confirm the conclusions of Athanasiadis et al. (2010) and Li and Wettstein (2012) that the NAO is connected with the latitudinal shift of the eddy-driven Atlantic jet and the PNA is mostly connected with variability in the strength of the subtropical Pacific jet. The profiles for the WP- and EA-patterns support mixed relationship with eddy-driven and subtropical jet variability for both, the WP-and EA-patterns. In contrast, the investigations of Li and Wettstein (2012) and Wettstein and Li (submitted to J. Climate) delivered evidence that the WP-pattern is related to eddy-driven jet variability and the EA signature revealed a mixed relationship with eddy-driven and subtropical jet variability.

5.2. *Simulated relation between major teleconnection patterns and zonal wind variability*

To gain deeper insights into the reasons of the limited skill of the CMIP3 ensemble in reproducing the spatial structure of teleconnection patterns, the simulated relation of the

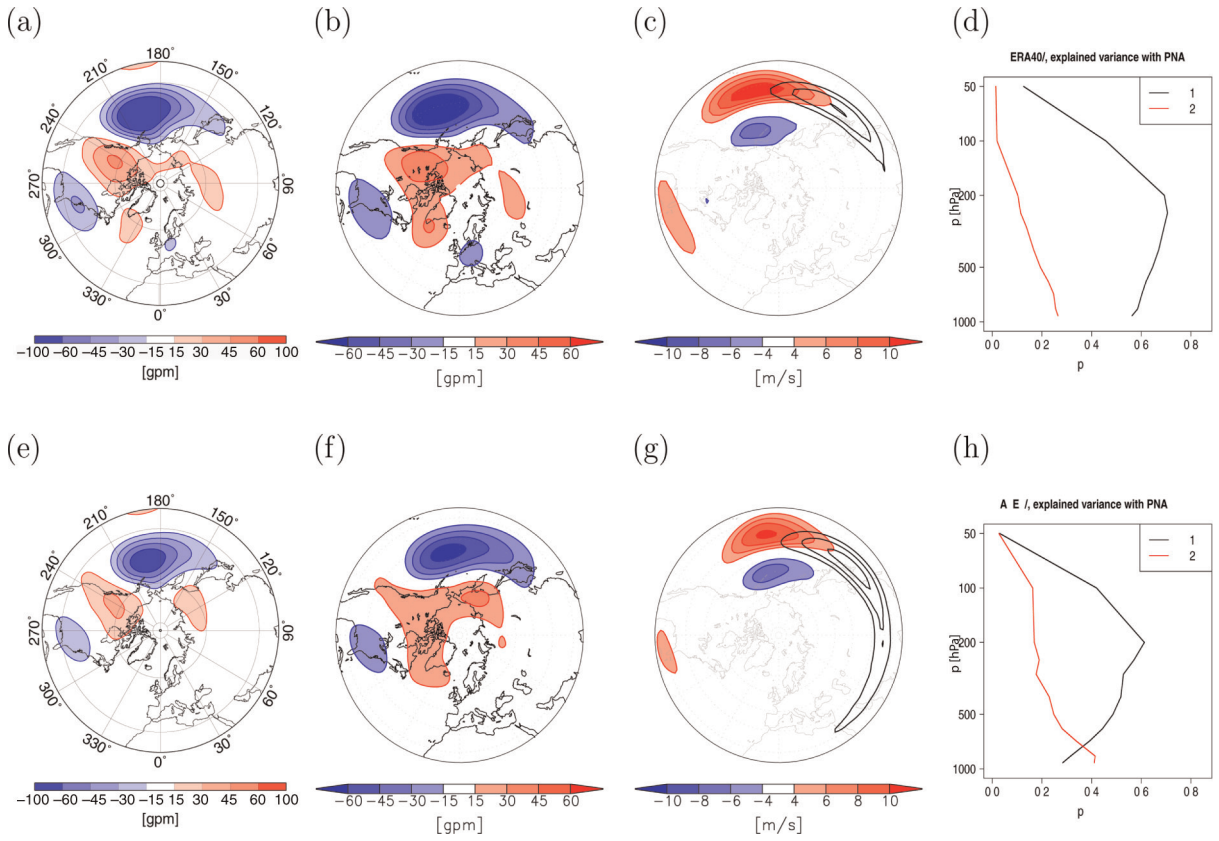

Fig. 16. Summary of the PNA patterns and their relation to PAC-*u*-EOF1 for ERA40 re-analysis (a–d) and UKMO HadGEM1 (e–h). DJF-data from 1958 to 1999. From left to right: the PNA pattern (a, e); the regression pattern of the global geopotential height field at 500hPa onto PAC-*u*-PC1 at 250hPa (b, f); the regression pattern of the global zonal wind field at 250hPa onto PAC-*u*-PC1 at 250hPa (colours with overlaid Pacific mean jet) (c, g); the vertical profile of explained variance between the PNA-index and the sectoral PAC-*u*-PC1 at each height (d, h).

four major teleconnection patterns with the zonal wind variability has been studied. The second row of the Figs. 14 to 17 summarises the dynamical relationships for the four most important teleconnection patterns NAO, EA, PNA and WP for one selected model of the CMIP3 ensemble, which simulated the spatial structure of the respective pattern reasonably well. The corresponding figures for two more models of the CMIP3 ensemble can be found in the supplement.

The observed zonal wind variability patterns at jet core heights are well reproduced by the selected models. In particular the Atlantic zonal wind variability patterns display changes in the position (ATL-*u*-EOF1) and in the strength of the Atlantic jets (ATL-*u*-EOF2). The simulated centres of action are found at similar locations as the observed ones, resulting in high pattern correlations between observed and simulated Atlantic zonal wind variability patterns (0.89 to 0.97 at 500 hPa and 0.85 to 0.97 at 250 hPa). Over the Pacific, the simulated zonal wind variability patterns display changes in the strength (PAC-*u*-EOF1) and in the position (PAC-*u*-EOF2) of the Pacific jets in the upper to middle troposphere. Again, the simulated centres of action are found at similar locations as the observed ones, resulting in high pattern correlations between observed and simulated Pacific zonal wind variability patterns (0.92 to 0.98 at 500 hPa and 0.88 to 0.97 at 250 hPa). The regression patterns of geopotential height fields at 500 hPa are very similar to the teleconnection patterns, underlining the close relation of the NAO/EA (PNA/WP) patterns to zonal wind variations over the Atlantic (Pacific).

Larger differences can be found for the vertical profiles of shared variance with the teleconnection indices. For all selected models, the first Atlantic *u*-PCs share the largest amount of their variance with the NAO-index. The general shape of the vertical profile is similar to that for the re-analysis data, displaying largest values of shared variance in the lower troposphere with a rather linear, though slight decrease throughout the troposphere. The second Atlantic *u*-PCs share the largest amount of their variance with the EA-index in accordance with the re-analysis data, but

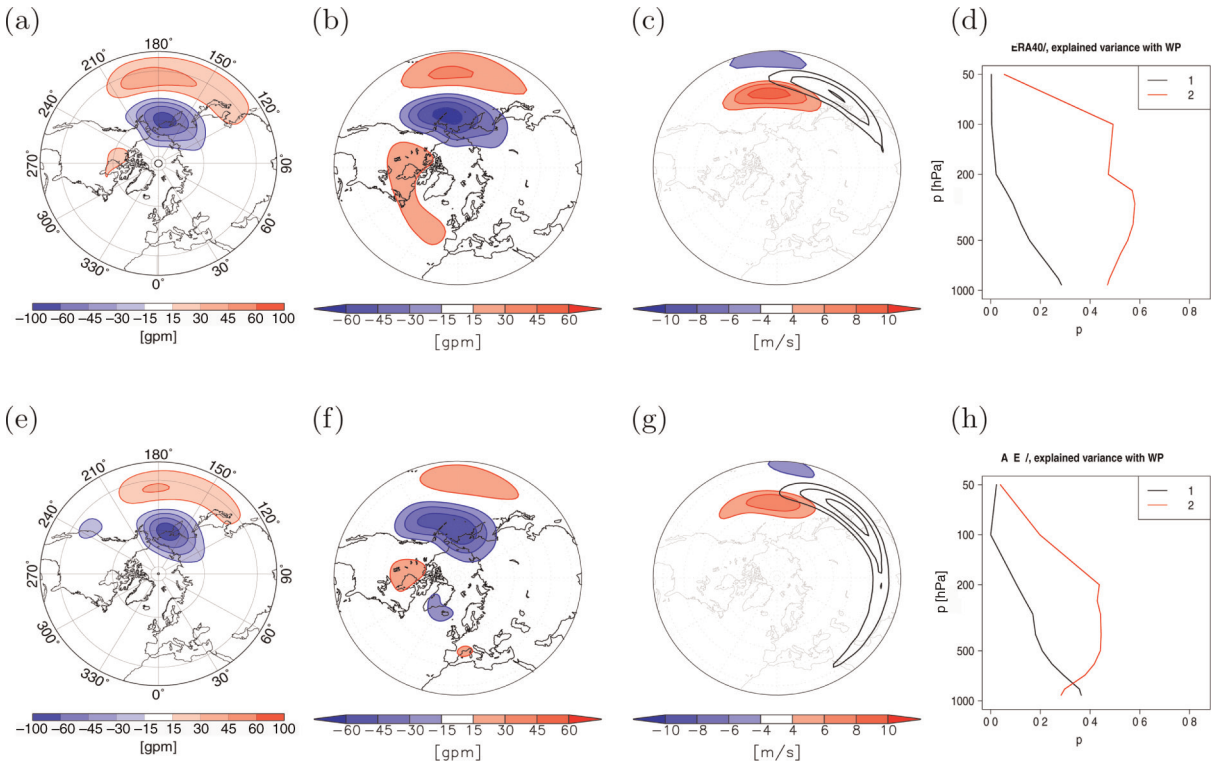

Fig. 17. Summary of the WP patterns and their relation to PAC-*u*-EOF2 for ERA40 re-analysis (a–d) and UKMO HadGEM1 (e–h). DJF-data from 1958 to 1999. From left to right: the WP pattern (a, e); the regression pattern of the global geopotential height field at 500hPa onto PAC-*u*-PC2 at 250hPa (b, f); the regression pattern of the global zonal wind field at 250hPa onto PAC-*u*-PC2 at 250hPa (colours with overlaid Pacific mean jet) (c, g); the vertical profile of explained variance between the WP-index and the sectoral PAC-*u*-PC2 at each height (d, h).

larger differences in the shape of the vertical profile occur. Having in mind the mixed relationship of EA with eddy-driven and subtropical jet variability proposed by Wettstein and Li (submitted to J. Climate), which is rather sensitive to small changes in the location of the centres of actions of the related *u*-EOF2, a greater variety of these profiles can be expected. The first Pacific *u*-PCs show the largest values of explained variance with the PNA-index, but not all models reproduce the same shape of the vertical profile as the re-analysis with a maximum in the upper troposphere indicating a relation to subtropical jet variability. Considering the WP-index of the re-analysis data, the shape of the vertical covariance profile indicates a mixed relationship rather than the eddy-driven jet variability shown by Wettstein and Li (submitted to J. Climate).

In order to assess the ability of the whole CMIP3 ensemble in simulating the dynamical relation between teleconnections and zonal wind variability we use the performance metrics introduced in section 3.4. Figs. 18 and 19 display the performance metrics for 23 CMIP3-models for the period from 1958 to 1999. The first three columns summarise from left to right the skill scores of the specific teleconnection pattern, the related patterns of zonal wind variability at 250 hPa determined by sectoral *u*-EOFs and the regression patterns of the global geopotential height field at 500 hPa onto the sectoral zonal wind PCs at 250 hPa. The fourth and fifth column describe the skill scores for the comparison of the regression patterns (regression of geopotential height field at 500 hPa onto the first and second sectoral zonal wind PCs at 250 hPa) with the teleconnection pattern of the same model. These scores indicate, whether and how closely the distinct teleconnection pattern is related to the first or second dominant pattern of zonal wind variability for the considered model. The models have been sorted according to the skill score for the particular teleconnection pattern.

These performance metrics give evidence for large differences in simulating the dynamical relation between teleconnections and zonal wind variability within the CMIP3 ensemble. But for every pattern there are about half or more models, which are able to reproduce a similar relationship as that obtained for the re-analysis data. To show this in more detail, the left columns of Figs. 20 and 21 present the same performance metrics as before in Figs. 18 and 19, but only for those models with a relation

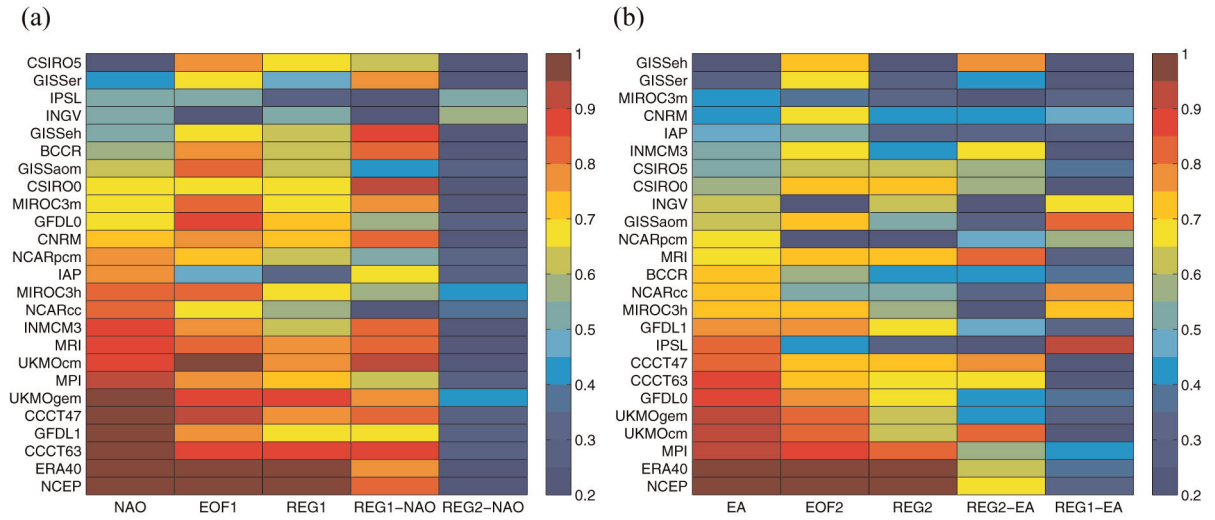

Fig. 18. Performance metrics for NAO (a) and EA (b) and their relations to ATL-*u*-EOFs. The columns of the metric give from left to right the values of the skill scores for teleconnection patterns, ATL-*u*-EOFs at 250hPa, regression patterns of the geopotential height field at 500hPa onto ATL-*u*-PC at 250hPa, comparison of teleconnection pattern and regression pattern of the same model. Models are sorted according to the skill score of the NAO and EA patterns, respectively.

between zonal wind variability and the major teleconnection patterns similar to that for the re-analysis data. That means NAO/EA connected with ATL-*u*-EOF1/ATL-*u*-EOF2; PNA/WP connected with PAC-*u*-EOF1/PAC-*u*-EOF2.

The relationships of NAO with ATL-*u*-EOF1 and PNA with PAC-*u*-EOF1 are reproduced by the majority of the models. For the NAO, almost all of these models display vertical profiles of shared variance with the first Atlantic *u*-PCs similar to the re-analysis indicating eddy-driven variability (see Fig. 20). For the PNA, the relation to subtropical jet variability is not as distinct as in the re-analysis data (see Fig. 21). The relations between the second most important patterns of sectoral *u*-variability and the teleconnection patterns display a much larger spread over the CMIP3 ensemble. The EA-ATL-*u*-EOF2 and WP-PAC-*u*-EOF2 relationships determined for the re-analysis data are reproduced only by about half of the models with large variations of the shape of the vertical profiles of shared variance between teleconnection indices and related *u*-PCs (see Figs. 20 and 21).

A general conclusion from the performance metrics displayed in Figs. 18–21 can be drawn: If the zonal wind variability described in terms of sectoral *u*-EOFs is related

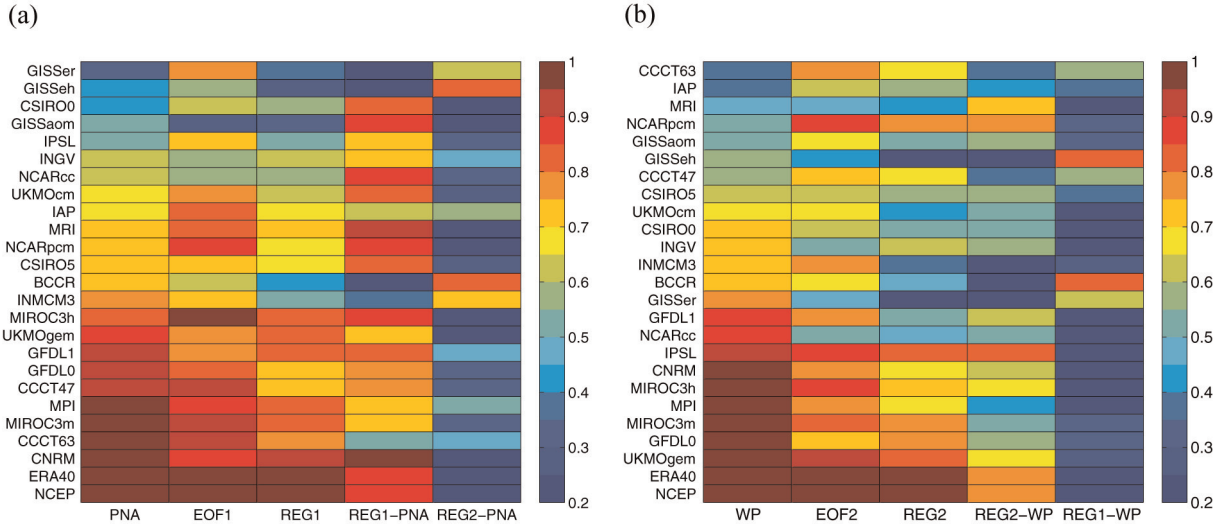

Fig. 19. Same as in Fig. 18, but for PNA (a) and WP (b) and their relations to PAC-*u*-EOFs. Models are sorted according to the skill score of the PNA and WP patterns, respectively.

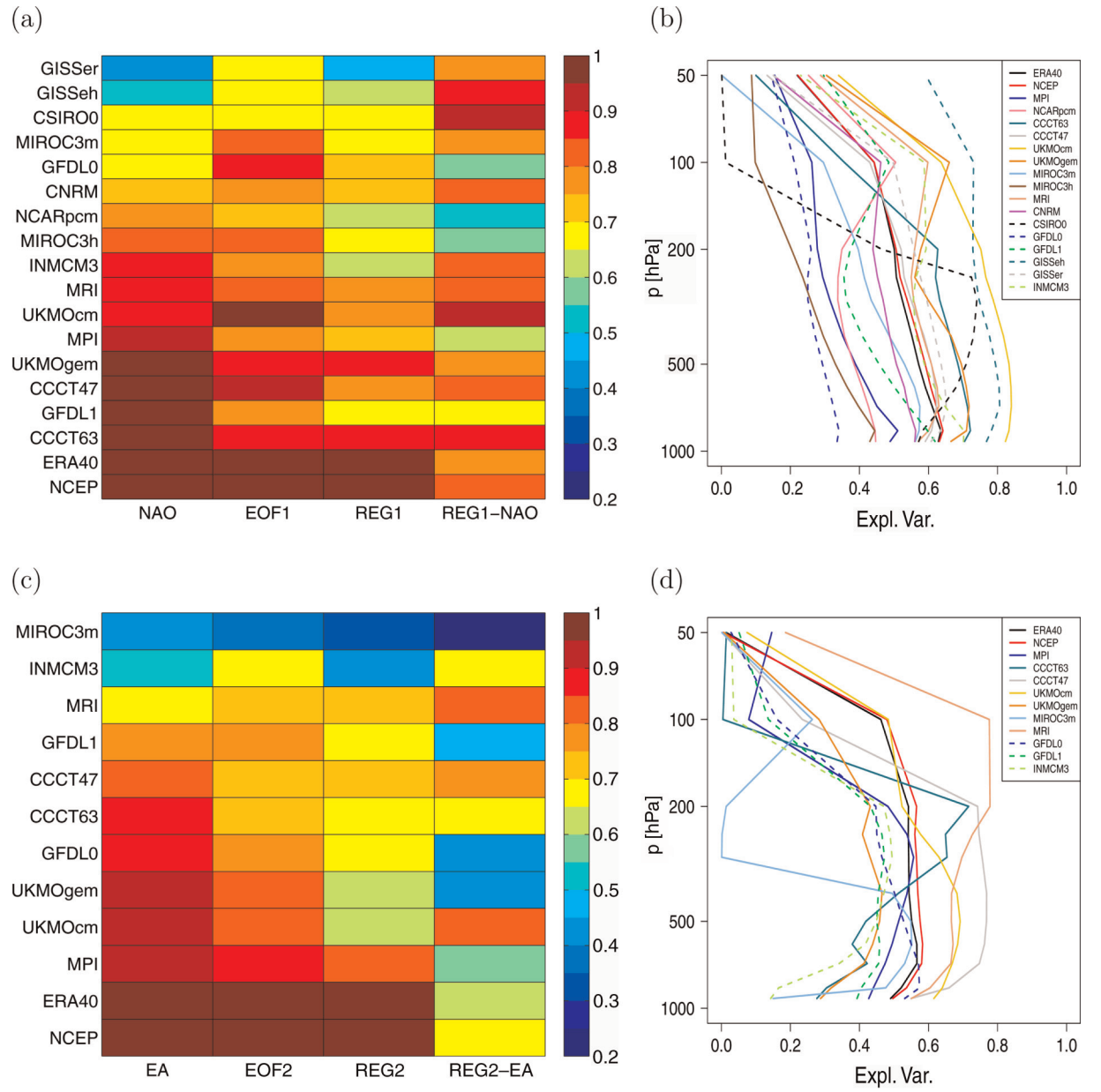

Fig. 20. Left: Performance metrics as in Fig. 18, but for those model showing same relationship between teleconnection and zonal wind variability as the re-analysis. Models are sorted according to the skill score of the NAO (a) and EA (c) patterns, respectively. (b, d) Vertical profiles of shared variance with the related ATL-*u*-PCs for the selected models.

to the main teleconnection patterns in the same way as for the re-analysis data then the quality of simulated teleconnection pattern is largely determined by the quality of the simulated zonal wind variability patterns.

5.3. *Conclusions*

The results of subsections 5.1 and 5.2 lead us to the conclusion that improvements of the skill of coupled climate models in reproducing teleconnections requires improvements in simulating the variability of zonal wind fields and their relation to atmospheric teleconnection patterns. The variability of zonal wind fields is largely determined by atmospheric eddy-mean flow interaction. Due to this interaction low frequency flow anomalies can be produced which interact with the high frequency transient eddies. The changed high frequency transient eddies can feed back upon the background zonal flow in

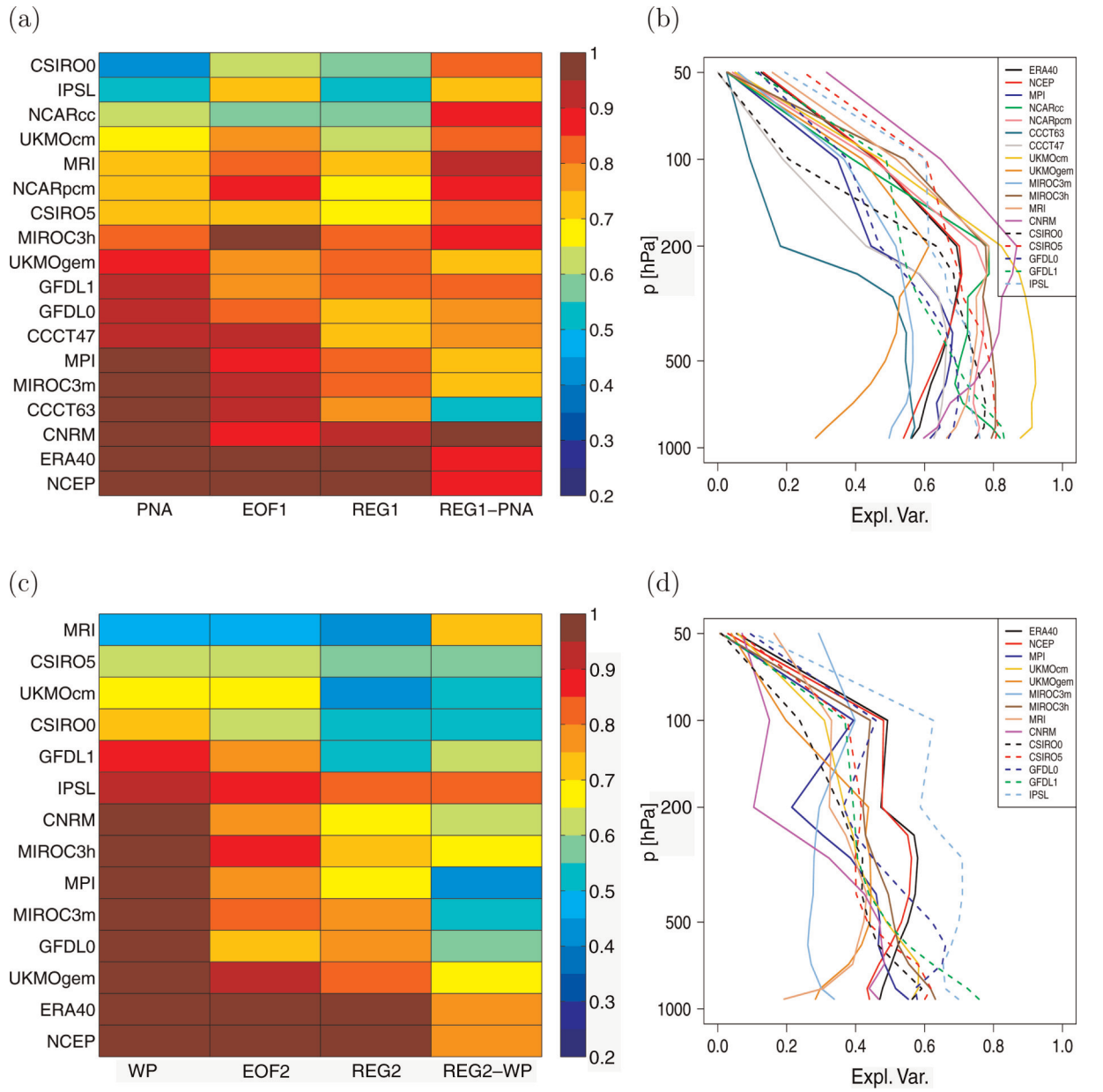

Fig. 21. Same as in Fig. 20 but for the PNA (a, b) and WP (c, d) patterns and their relation to PAC-*u*-EOFs. Models are sorted according to the skill score of the PNA and WP patterns, respectively.

different ways, preserving the existing anomaly patterns or generating changes of the background flow. Evidence for such a coupling between the high frequency transient eddies (baroclinic waves) and teleconnection patterns was given already by Lau (1988) and Lorenz and Hartmann (2001, 2003). The co-variability of zonal wind and baroclinic wave activity and their relation to the most dominant teleconnection patterns (NAO, PNA, WP and EA) has been investigated by, for example, Strong and Davis (2008), Athanasiadis et al. (2010) and Woollings et al. (2010). They showed that the co-variability structures detected for the re-analysis data are qualitatively similar in the Atlantic and Pacific sectors.

To conclude from the investigations of this section, a better understanding of the dynamical reasons for limited skill of the CMIP3 ensemble in reproducing teleconnections requires a detailed analysis of the simulated eddy-mean flow interaction, e.g. by studying the simulated co-variability of zonal wind and baroclinic wave activity and by analysing the related localised Eliassen-Palm fluxes

(Trenberth, 1986). Depending on data availability, this will be explored in future.

6. Summary and outlook

Atmospheric teleconnections describe important aspects of the low-frequency atmospheric variability on time-scales of months and longer. In the light of the increased need to provide reliable statements about seasonal to decadal predictability, it is necessary that state-of-the-art climate models simulate the spatial and temporal behaviour of atmospheric teleconnections satisfactorily. Therefore, an evaluation of climate models requires the evaluation of the simulated climate variability in terms of teleconnection patterns.

6.1. Summary

Our study presented the results of such an evaluation of present-day coupled simulations performed with the CMIP3-multi-model ensemble. The comprehensive evaluation has been performed for the period 1958–1999, for which reliable re-analysis data are available for comparison. For the shorter period from 1979 to 1999 atmosphere-only model simulations (AMIP3 simulations) are available for a subset of the multi-model ensemble which have been also analysed.

Regarding the spatial variability of the atmospheric teleconnections our analyses revealed:

- The spatial patterns of the most important teleconnections are reproduced reasonably by most of the models but the strength of the centres of action varies among the model runs. The coupled climate models reproduce the most dominant NAO and PNA patterns best for the longer period 1958–1999. Thus, our study confirms the spatial pattern reproduction estimated by Stoner et al. (2009) for the winter NAO- and PNA-pattern and by Casado and Pastor (2012) for the North-Atlantic teleconnections NAO, SCAN, EA, EA/WR.
- The models show a general tendency to reproduce the Pacific patterns better than the Atlantic patterns, but some models show large discrepancies in their ability to reproduce the patterns for the Atlantic or the Pacific sectors. Three models (UKMO HadGEM1, ECHAM5/MPI-OM1, GFDL CM2.1) reproduce the Atlantic as well as the Pacific patterns very well.
- For all patterns, the performance of the coupled models in reproducing the spatial patterns is generally worse for the shorter period 1979–1999.
- The comparison of the AMIP3- and CMIP3-ensemble for the short period from 1979 to 1999 confirmed that the influence of the forcing by SST anomalies on the spatial structure of atmospheric variability patterns is rather small for most of the patterns. Only for three wave-train like patterns (EA/WR, SCAN, PNA) the AMIP3 ensemble has slightly improved skill in reproducing the spatial structure, indicating that a better representation of the SST forcing has the potential to improve (at least slightly) the simulation of wave-train like atmospheric teleconnection patterns.

By analysing the temporal behaviour of atmospheric teleconnections we arrived at the following results:

- Current state-of-the-art climate models are not able to reproduce the temporal behaviour, in particular the exact phasing of the dominant patterns due to internally generated model variability.
- The state-of-the-art climate models are not able to capture the observed frequency behaviour and characteristic time scales for the coupled runs satisfactorily. For the NAO time-series, only a few models display the observed enhanced energy at quasi-decadal scale. For the PNA time-series, the enhanced spectral energy on inter-annual scales is captured by many models, even though mostly with smaller magnitude. These results are in accordance with Stoner et al. (2009) and Casado and Pastor (2012). Both studies concluded that the models are not able to reproduce the temporal characteristics of atmospheric teleconnection time-series. Furthermore, Stoner et al. (2009) estimated as the best reproducible feature of temporal behaviour the enhanced spectral energy on inter-annual scale for the PNA time-series.
- For the atmosphere-only runs, the reproduction of the enhanced spectral energy on inter-annual time-scales of the PNA time-series is considerably improved for the majority of models.

The investigations on the dynamical reasons for the limited skill of the multi-model-CMIP3 ensemble in reproducing atmospheric teleconnections resulted in:

- There is a large spread in simulating the dynamical relation between the four major teleconnection patterns NAO, EA, PNA and WP and the sectoral zonal wind variability over the CMIP3 ensemble. But for every teleconnection pattern there are about half or more models, which are able to reproduce a similar relationship as that obtained for the re-analysis data.

- The vertical profiles of shared variance between the teleconnection time-series and the time-series of the corresponding zonal wind variability patterns display characteristic shapes indicating eddy-driven variability (for the NAO), subtropical jet variability (for the PNA) or variability of mixed character (for WP and EA). For the NAO, almost all models which reproduce the dynamical relation between zonal wind variability and the NAO teleconnection display vertical profiles of shared variance similar to the re-analysis indicating eddy-driven variability. For the PNA, the simulated relation to subtropical jet variability is not as distinct as for the re-analysis data. For the EA and WP patterns large variations of the shape of the vertical profiles of shared variance have been detected.
- If the zonal wind variability described in terms of sectoral EOFs of zonal wind is related to the main teleconnection patterns in the same way as for the re-analysis data then the quality of simulated teleconnection pattern is largely determined by the quality of the simulated zonal wind variability patterns.

6.2. *Outlook*

We conclude that a better representation of the zonal wind variability and of the dynamical relation between zonal wind variability and the major atmospheric teleconnections has the potential to further improve the simulated low-frequency flow variability. The eddy-mean flow interaction can lead to different states of the large-scale anomalies, the maintenance of the existing anomaly patterns (e.g. a positive NAO-state) or the transition to a new anomaly pattern (e.g. a negative NAO-state). Evidence for such a coupling between the high frequency transient eddies and teleconnection patterns was given already by Lau (1988), Lorenz and Hartmann (2001, 2003) and Sempf et al. (2005). Recent work elaborated the role of synoptic-scale Rossby wave breaking for such transitions (e.g. Benedict et al., 2004; Franzke et al., 2004; Woollings et al., 2008; Riviere, 2010; Riviere et al., 2010; Franzke et al., 2011b).

It has long been observed that some of these distinct large-scale anomaly patterns occur more frequently than others. This observation provides a framework for the understanding of low-frequency variability that arises due to transitions between the preferred large-scale anomaly patterns, called atmospheric flow regimes (Palmer, 1999). Pronounced regime behaviour has also been estimated for coupled climate models (e.g. Handorf et al., 2009). To prove the existence of atmospheric flow regimes one has to understand the underlying dynamical mechanisms. For simplified atmospheric models, as well barotropic and baroclinic models, it was shown that regimes are associated with the large-scale structure of the underlying chaotic attractor (e.g. Itoh and Kimoto, 1996; Sempf et al., 2007a, 2007b). In particular, for the Northern Hemisphere wintertime atmospheric circulation simulated by a baroclinic quasi-geostrophic model, Sempf et al. (2007a, 2007b) have proven that these atmospheric regimes are due to chaotic itinerancy between attractor ruins. By changing surface friction or turbulent friction between the atmospheric layers the large-scale structure of the merged attractor can be changed which is related to changes in the regime behaviour.

The eddy-mean flow interaction play a fundamental role for the representation of atmospheric teleconnections as well as for atmospheric regime transitions and hence low-frequency variability. As shown in several studies and mentioned above, in particular the synoptic-scale Rossby wave breaking drives not only most atmospheric teleconnection patterns (Feldstein, 2003; Benedict et al., 2004; Franzke et al., 2004; Riviere and Orlanski, 2007; Woollings et al., 2008; Franzke et al., 2011a) but also transitions between atmospheric flow regimes (Benedict et al., 2004; Franzke et al., 2004; Woollings et al., 2008; Riviere, 2010; Riviere et al., 2010; Franzke et al., 2011b).

Our results deliver hints on model deficiencies in simulating the synoptic eddy-mean flow interactions correctly. A detailed analysis of the simulated eddy-mean flow interaction can be done by, e.g. the related localised Eliassen-Palm fluxes (Trenberth, 1986). Depending on data availability, this will be explored in future, similar to Jaiser et al. (2012).

Based on the results of this study we suggest that an improved representation of atmospheric teleconnections in global coupled climate and Earth system models requires a much higher horizontal model resolutions and a more realistic description of the synoptic-scale mean-flow interactions, which also implies the development of adapted and improved physical sub-grid scale parameterisations.

Based on this study and in the light of the strong need to provide reliable assessments of decadal predictability, the potential of atmospheric teleconnections for decadal predictability needs further investigations. This requires a better understanding of the underlying mechanisms of variability patterns and flow regimes, an improvement of the skill of state-of-the-art climate and Earth system models in reproducing atmospheric teleconnections and the identification of sources for long-range predictive skill of teleconnections. The latter may be provided by initial and boundary conditions provided by the ocean to the atmosphere, by troposphere-stratosphere interactions, or by changes in the land-surface or sea-ice conditions.

7. Acknowledgments

We acknowledge the modelling groups, the Program for Climate Model Diagnosis and Intercomparison (PCMDI) and the WCRP's Working Group on Coupled Modelling (WGCM) for their roles in making available the WCRP CMIP3 multi-model data set. Support of this dataset is provided by the Office of Science, US Department of Energy. We would like to thank NOAA, Earth System Research Laboratory, Physical Sciences Division, Boulder for providing the NCEP Reanalysis derived data and the European Centre for Medium Range Weather Forecast for providing the ERA40 Reanalysis data. Wavelet software was provided by C. Torrence and G. Compo and is available at http://atoc.colorado.edu/research/wavelets/. For parts of the calculations and graphics we have applied the free software package R and we would like to appreciate the efforts of the team of developers of R and all package writers to maintain and develop this valuable source of free software. We are particularly grateful to Sabine Erxleben for conducting data analysis and preparing the figures. We are grateful to two anonymous reviewers for thorough reviews.

References

Ambaum, M. H. P., Hoskins, B. J. and Stephenson, D. B. 2001. Arctic oscillation or North Atlantic oscillation? *J. Climate*. **14**, 3495–3507.

Athanasiadis, P. J. and Ambaum, M. H. P. 2009. Linear contributions of different time scales to teleconnectivity. *J. Climate*. **22**, 3720–3728.

Athanasiadis, P. J., Wallace, J. M. and Wettstein, J. J. 2010. Patterns of wintertime jet stream variability and their relation to the storm tracks. *J. Atmos. Sci*. **67**, 1361–1381.

Barbosa, S., Silva, M. E. and Fernandes, M. J. 2006. Wavelet analysis of the Lisbon and Gibraltar North Atlantic Oscillation winter indices. *Int. J. Climatol*. **26**, 581–593.

Barnston, A. G. and Livezey, R. E. 1987. Classification, seasonality and persistence of low-frequency atmospheric circulation patterns. *Mon. Wea. Rev*. **115**, 1083–1126.

Benedict, J. J., Lee, S. and Feldstein, S. B. 2004. Synoptic view of the North Atlantic Oscillation. *J. Atmos. Sci*. **61**, 121–144.

Blackmon, M. L., Lee, Y. H. and Wallace, J. M. 1984. Horizontal structure of 500-mb height fluctuations with long, intermediate and short-time scales. *J. Atmos. Sci*. **41**, 961–979.

Casado, M. and Pastor, M. 2012. Use of variability modes to evaluate AR4 climate models over the Euro-Atlantic region. *Clim. Dyn*. **38**, 225–237.

Dickson, R. R. and Namias, J. 1976. North American influences on the circulation and climate of the North Atlantic sector. *Mon. Wea. Rev*. **104**, 1255–1265.

Feldstein, S. B. 2003. The dynamics of NAO teleconnection pattern growth and decay. *Quart. J. Roy. Meteor. Soc*. **129**, 901–924.

Franzke, C., Feldstein, S. B. and Lee, S. 2011a. Synoptic analysis of the Pacific-North American teleconnection pattern. *Quart. J. Roy. Meteor. Soc*. **137**, 329–346.

Franzke, C., Lee, S. and Feldstein, S. B. 2004. Is the North Atlantic Oscillation a breaking wave? *J. Atmos. Sci*. **61**, 145–160.

Franzke, C., Woollings, T. and Martius, O. 2011b. Persistent circulation regimes and preferred regime transitions in the North Atlantic. *J. Atmos. Sci*. **68**, 2809–2825.

Gan, T. Y., Gobena, A. K. and Wang, Q. 2007. Precipitation of southwestern Canada: wavelet, scaling, multifractal analysis, and teleconnection to climate anomalies. *J. Geophys. Res*. **112**, D10110.

Glowienka-Hense, R. 1990. The North Atlantic Oscillation in the Atlantic-European SLP. *Tellus*. **42A**, 497–507.

Handorf, D., Dethloff, K., Marshall, A. G. and Lynch, A. 2009. Climate regime variability for past and present time slices simulated by the Fast Ocean Atmosphere Model. *J. Climate*. **22**, 58–70.

Handorf, D., Petoukhov, V. K., Dethloff, K., Eliseev, A. V., Weisheimer, A. and co-authors. 1999. Decadal climate variability in a coupled atmosphere-ocean climate model of moderate complexity. *J. Geophys. Res*. **104**, 27253–27276.

Hannachi, A., Jolliffe, I. T. and Stephenson, D. B. 2007. Empirical orthogonal functions and related techniques in atmospheric science: a review. *Int. J. Climatol*. **27**, 1119–1152.

Hoskins, B. J. and Karoly, D. J. 1981. The steady linear response of a spherical atmosphere to thermal and orographic forcing. *J. Atmos. Sci*. **38**, 1179–1196.

Hurrell, J. W. 1996. Influence of variations in extratropical wintertime teleconnections on Northern Hemisphere temperature. *Geophys. Res. Lett*. **23**, 665–668.

Hurrell, J. W. and van Loon, H. 1997. Decadal variations in climate associated with the North Atlantic Oscillation. *Clim. Change*. **36**, 301–326.

Huth, R. 1997. Continental-scale circulation in the UKHI GCM. *J. Climate*. **10**, 1545–1561.

Itoh, H. and Kimoto, M. 1996. Multiple attractors and chaotic itinerancy in a quasigeostrophic model with realistic topography: implications for weather regimes and low-frequency variability. *J. Atmos. Sci*. **53**, 2217–2231.

Jaiser, R., Dethloff, K., Handorf, D., Rinke, A. and Cohen, J. 2012. Impact of sea ice cover changes on the Northern Hemisphere atmospheric winter circulation. *Tellus A*. **64**, 11595.

Kalnay, E., Kanamitsu, M., Kistler, R., Collins, W., Deaven, D. and co-authors. 1996. The NCEP/NCAR 40-year reanalysis project. *Bull. Amer. Meteor. Soc*. **77**, 437–470.

Kushnir, Y., Robinson, W. A., Blade, I., Hall, N. M. J., Peng, S. and co-authors. 2002. Atmospheric GCM response to extratropical SST anomalies: synthesis and evaluation. *J. Climate*. **15**, 2233–2256.

Kuzmina, S. I., Bengtsson, L., Johannessen, O. M., Drange, H., Bobylev, L. P. and co-authors. 2005. The North Atlantic Oscillation and greenhouse-gas forcing. *Geophys. Res. Lett*. **32**, L04 703.

Lau, N.-C. 1988. Variability of the observed midlatitude storm tracks in relation to low-frequency changes in the circulation pattern. *J. Atmos. Sci*. **45**, 2718–2743.

Li, C. and Wettstein, J. J. 2012. Thermally-driven and eddy-driven jet variability in reanalysis. *J. Climate*. **25**, 1587–1596.

Lorenz, D. J. and Hartmann, D. L. 2001. Eddy-zonal flow feedback in the Southern Hemisphere. *J. Atmos. Sci.* **58**, 3312–3327.

Lorenz, D. J. and Hartmann, D. L. 2003. Eddy-zonal flow feedback in the Northern Hemisphere winter. *J. Climate*. **16**, 1212–1227.

Marshall, J., Kushnir, J., Battisti, D., Chang, P., Czaja, A. and co-authors. 2001. North Atlantic climate variability: phenomena, impacts and mechanisms. *Int. J. Climatol.* **21**, 1863–1898.

Meehl, G., Covey, C., Delworth, T., Latif, M., McAvaney, B. and co-authors. 2007. The WCRP CMIP3 multi-model dataset: a new era in climate change research. *Bull. Amer. Meteor. Soc.* **88**, 1383–1394.

Nakamura, H., Sampe, T., Tanimota, Y. and Shimpo, A. 2004. Observed associations among storm tracks, jet streams and midlatitude oceanic fronts. *Geophys. Monogr.* **147**, 329–345.

Palmer, T. N. 1999. A nonlinear dynamical perspective on climate prediction. *J. Climate*. **12**, 575–591.

Panagiotopoulos, F., Shahgedanova, M. and Stephenson, D. B. 2002. A review of Northern Hemisphere winter-time teleconnection patterns. *J de Physique IV, EDP Sci.* **12**, 1027–1047.

Preisendorfer, R. 1988. *Principal Component Analysis in Meteorology and Oceanography (Developments in Atmospheric Science, Vol. 17)*. Elsevier, Amsterdam, p. 425.

Reichler, T. and Kim, J. 2008. How well do coupled models simulate today's climate? *Bull. Amer. Meteor. Soc.* **89**, 303–311.

Renshaw, A. C., Rowelland, D. P. and Folland, C. K. 1998. Wintertime low-frequency weather variability in the North Pacific-American section. *J. Climate*. **11**, 1073–1093.

Richman, M. B. 1986. Rotation of principal components. *J. Climatol.* **6**, 293–335.

Riviere, G. 2010. Role of Rossby wave breaking in the west Pacific teleconnection. *Geophys. Res. Lett.* **37**, L11802.

Riviere, G., Laine, A., Lapeyre, G., Salas-Melia, D. and Kageyama, M. 2010. Links between Rossby wave breaking and the North Atlantic Oscillation-Arctic oscillation in present-day and last glacial maximum climate simulations. *J. Climate*. **23**, 2987–3008.

Riviere, G. and Orlanski, I. 2007. Characteristics of the Atlantic storm-track eddy activity and its relation with the North Atlantic Oscillation. *J. Atmos. Sci.* **64**, 241–266.

Sempf, M., Dethloff, K., Handorf, D. and Kurgansky, M. V. 2005. Idealized modelling of the northern annular mode: orographic and thermal impacts. *Atmos. Sci. Lett.* **6**, 140–144.

Sempf, M., Dethloff, K., Handorf, D. and Kurgansky, M. V. 2007a. Circulation regimes due to attractor merging in atmospheric models. *J. Atmos. Sci.* **64**, 2029–2044.

Sempf, M., Dethloff, K., Handorf, D. and Kurgansky, M. V. 2007b. Toward understanding the dynamical origin of atmospheric regime behavior in a baroclinic model. *J. Atmos. Sci.* **64**, 887–904.

Shin, S.-I. and Sardeshmukh, P. D. 2011. Critical influence of the pattern of Tropical Ocean warming on remote climate trends. *Clim. Dyn.* **36**, 1577–1591.

Stephenson, D. B. and Pavan, V. 2003. The North Atlantic Oscillation in coupled climate models: a CMIP1 evaluation. *Clim. Dyn.* **20**, 381–399.

Stephenson, D. B., Pavan, V., Collins, M., Junge, M. M., Quadrelli, R. and Participating CMIP2 Modelling Group. 2006. North Atlantic Oscillation response to transient greenhouse gas forcing and the impact on European winter climate: a CMIP2 multi-model assessment. *Clim. Dyn.* **27**, 401–420.

Stoner, A. M. K., Hayhoe, K. and Wuebbles, D. J. 2009. Assessing general circulation model simulations of atmospheric teleconnection patterns. *J. Climate*. **22**, 4348–4372.

Straus, D. M. and Shukla, J. 2002. Does ENSO force the PNA? *J. Climate*. **15**, 2340–2358.

Strong, C. and Davis, R. E. 2008. Variability in the position and strength of winter jet stream cores related to northern hemisphere teleconnections. *J. Climate*. **21**, 584–592.

Taylor, K. E. 2001. Summarizing multiple aspects of model performance in a single diagram. *J. Geophys. Res.* **106**, 7183–7192.

Torrence, C. and Compo, G. P. 1998. A practical guide to wavelet analysis. *Bull. Amer. Meteor. Soc.* **79**, 61–78.

Trenberth, K. E. 1986. An assessment of the impact of transient eddies on the zonal flow during a blocking episode using localized Eliassen-Palm flux diagnostics. *J. Atmos. Sci.* **43**, 2070–2087.

Uppala, S. M., KÅllberg1, P. W., Simmons1, A. J., Andrae1, U., Da Costa Bechtold1, V. and co-authors. 2005. The ERA-40 re-analysis. *Quart. J. Roy. Meteor. Soc.* **131**, 2961–3012.

Vallis, G. K. 2006. *Atmospheric and Oceanic Fluid Dynamics. Fundamentals and Large-Scale Circulation*. Cambridge University Press, Cambridge, UK, p. 745.

Vallis, G. K. and Gerber, E. P. 2008. Local and hemispheric dynamics of the North Atlantic Oscillation, annular patterns and the zonal index. *Dyn. Atmos. Oceans.* **44**, 184–212.

Von Storch, H. and Zwiers, F. W. 1999. *Statistical Analysis in Climate Research*. Cambridge University Press, Cambridge, UK, p. 484.

Walker, G. T. and Bliss, E. W. 1932. World weather V. *Mem. R. Meteor. Soc.* **4**, 53–84.

Wallace, J. M. and Gutzler, D. S. 1981. Teleconnections in the geopotential height field during the Northern Hemisphere winter. *Mon. Wea. Rev.* **109**, 784–812.

Wanner, H., Brönnimann, S., Casty, C., Gyalistras, D., Luterbacher, J. and co-authors. 2001. North Atlantic Oscillation – Concepts and studies. *Surveys Geophys.* **22**, 321–382.

Wettstein, J. J. and Li, C. Submitted to J. Climate. Eddy-driven and subtropically-influenced jet variability structures in the observed three-dimensional zonal wind field. *J. Climate*.

Woollings, T., Hannachi, A. and Hoskins, B. 2010. Variability of the North Atlantic eddy-driven jet stream. *Quart. J. Roy. Meteor. Soc.* **136**, 856–868.

Woollings, T., Hoskins, B., Blackburn, M. and Berrisford, P. 2008. A new Rossby wave-breaking interpretation of the North Atlantic Oscillation. *J. Atmos. Sci.* **65**, 609–626.

Wunsch, C. 1999. The interpretation of short climate records, with comments on the North Atlantic and Southern Oscillations. *Bull. Amer. Meteor. Soc.* **80**, 245–255.

Yu, B., Shabbar, A. and Zwiers, F. W. 2007. The enhanced PNA-like climate response to Pacific interannual and decadal variability. *J. Climate*. **20**, 5285–5300.

Yu, B., Tang, Y. M., Zhang, X. B. and Niitsoo, A. 2009. An analysis on observed and simulated PNA associated atmospheric diabatic heating. *Clim. Dyn.* **33**, 75–91.

Yu, B. and Zwiers, F. W. 2007. The impact of combined ENSO and PDO on the PNA climate. A 1000-year climate modeling study. *Clim. Dyn.* **29**, 837–851.